TIMP1 mediates astrocyte-dependent local immunosuppression in brain metastasis acting on infiltrating CD8+ T cells

(Article begins on next page)

27 November 2024

TIMP1 mediates astrocyte-dependent local immunosuppression in brain metastasis acting on infiltrating CD8+ T cells.

*Running title: Astrocyte-dependent immunosuppression in brain metastasis.

Neibla Priego[1*], Ana de Pablos-Aragoneses[1], María Perea-García[1], Valentina Pieri[1+], Carolina Hernández-Oliver[1], Laura Álvaro-Espinosa[1], Andrea Rojas[1@], Oliva Sánchez[1], Ariane Steindl[1$], Eduardo Caleiras[2], Fernando García[3], Santiago García-Martín[4], Osvaldo Graña-Castro[4#], Sandra García-Mulero[5,6], Diego Serrano[7], Paloma Velasco-Beltrán[8,] Borja Jiménez-Lasheras[8], Leire Egia-Mendikute[8], Luise Rupp[9], Antonia Stammberger[9], Matthias Meinhardt[10], Anas Chaachou-Charradi[11], Elena Martínez-Saez[11], Luca Bertero[12,13], Paola Cassoni[12,13], Luca Mangherini[12,13], Alessia Pellerino[14], Roberta Rudà[14], Riccardo Soffietti[15], Fatima Al-Shahrour[4], Paul Saftig[16], Rebeca Sanz-Pamplona[5,17,18], Marc Schmitz[9,19,20], Stephen J Crocker[21], Alfonso Calvo[7], Asís Palazón[8,22], RENACER[23], Manuel Valiente[1*].

1 Brain Metastasis Group, Spanish National Cancer Research Centre (CNIO), Madrid, Spain.
2 Histopathology Unit, Spanish National Cancer Research Centre (CNIO), Madrid, Spain.
3 Proteomics Unit, Spanish National Cancer Research Centre (CNIO), Madrid, Spain.
4 Bioinformatics Unit, Spanish National Cancer Research Centre (CNIO), Madrid, Spain.
5 Biomarkers and Susceptibility Unit, Oncology Data Analytics Program (ODAP), Catalan Institute of Oncology (ICO), Bellvitge Biomedical Research Institute (IDIBELL), L'Hospitalet de Llobregat, Spain.
6 Department of Pathology and Experimental Therapy, School of Medicine, University of Barcelona (UB), L'Hospitalet de Llobregat, Barcelona, Spain.
7 Center for Applied Clinical Research (CIMA); Department of Pathology, Anatomy and Physiology, Faculty of Medicine, University of Navarra; IdISNA, Pamplona, Spain; CIBERONC, Madrid, Spain.
8 Cancer Immunology and Immunotherapy Lab, Center for Cooperative Research in Biosciences (CIC BioGUNE), Basque Research and Technology Alliance (BRTA), Derio, Spain.
9 Institute of Immunology, Faculty of Medicine Carl Gustav Carus, TU Dresden, Dresden, Germany.
10 Department of Pathology, Faculty of Medicine Carl Gustav Carus, TU Dresden, Dresden, Germany.
11 Pathology Department, Vall d'Hebron Hospital, Barcelona, Spain.
12 Department of Medical Sciences, University of Turin, Turin, Italy.
13 Pathology Unit, Department of Laboratory Medicine, Città della Salute e della Scienza University Hospital, Turin, Italy.
14 Division of Neuro-Oncology, Department of Neuroscience " Rita Levi Montalcini", University and City of Health and Science Hospital, Turin, Italy.
15 Candiolo Cancer Institute, FPO-IRCCS, Candiolo, Turin, Italy.
16 Biochemical Institute, Christian-Albrechts-Universität Kiel, Kiel, Germany.
17 University Hospital Lozano Blesa, Aragon Health Research Institute (IISA), ARAID Foundation, Aragon Government, Zaragoza, Spain.

50   18 Centro de Investigación Biomédica en Red de Epidemiologia y Salud Pública
51   (CIBERESP), Spain.
52   19 National Center for Tumor Diseases (NCT) Dresden, Dresden, Germany.
53   20 German Cancer Consortium (DKTK), partner site Dresden, and German Cancer
54   Research Center (DKFZ), Heidelberg, Germany.
55   21 Department of Neuroscience, University of Connecticut School of Medicine,
56   Farmington, USA.
57   22 Ikerbasque, Basque Foundation for Science, Bizkaia, Spain.
58   23 Biobank, Spanish National Cancer Research Centre (CNIO), Madrid, Spain.
59
60   #Current address: Instituto de Medicina Molecular Aplicada (IMMA) Nemesio Díez,
61   Basic Medical Science Department, Medicine School, Universidad San Pablo-CEU,
62   CEU Universities, Boadilla del Monte. Spain.
63   +Current address: Vita-Salute San Raffaele University, Milan, Italy.
64   @ Current address: School of Medicine, University Autónoma, Madrid, Spain.
65    $Current address: Division of Oncology, Department of Medicine I, Medical
66   University of Vienna, Vienna, Austria.
67   *Corresponding author
68
69   **Corresponding author information:**
70
71   Manuel Valiente
72   Spanish National Cancer Research Centre (CNIO), C/ Melchor Fernández Almagro,
73   3, 28029, Madrid, Spain.
74   mvaliente@cnio.es
75   +34 917 328 000 ext. 3035
76
77   Neibla Priego
78   Spanish National Cancer Research Centre (CNIO), C/ Melchor Fernández Almagro,
79   3, 28029, Madrid, Spain.
80   npriego@cnio.es
81   +34 917 328 000 ext. 3031
82
83   **Declaration of interests**
84   The authors declare no conflict of interest
85
86

2

87 **Abstract**

88

89 Immunotherapies against brain metastases have shown clinical benefits when
90 applied to asymptomatic patients, but they are largely ineffective in symptomatic
91 cases for unknown reasons. Here we dissect the heterogeneity in metastasis-
92 associated astrocytes using scRNAseq and report a population that blocks the
93 antitumoral activity of infiltrating T cells. This pro-tumoral activity is mediated by the
94 secretion of TIMP1 from a cluster of pSTAT3$^+$ astrocytes that acts on CD63$^+$ CD8$^+$ T
95 cells to modulate their function. Using genetic and pharmacologic approaches in
96 mouse and human brain metastasis models, we demonstrate that combining
97 immune checkpoint blockade antibodies with the inhibition of astrocyte-mediated
98 local immunosuppression may benefit patients with symptomatic brain metastases.
99 We further reveal that the presence of TIMP1 in liquid biopsies provides a biomarker
100 to select patients for this combined immunotherapy. Overall, our findings
101 demonstrate an unexpected immunomodulatory role for astrocytes in brain
102 metastases with clinical implications.

103

104 **State of significance**

105

106 This study presents a significant advance in the understanding of immunomodulation
107 in brain tumors and offers new insights into the potential therapeutic interventions for
108 brain metastases.

Introduction

The general dismal diagnosis of brain metastasis is starting to evolve into a more complex situation where significant differences in prognosis exist depending on the state of the disease (i.e., local only versus local and systemic) (1), or the presence of vulnerabilities for which specific targeted drugs have demonstrated substantial benefits (1). Similarly, immunotherapies based on immune checkpoint blockade (ICB) have been proved equally effective both on intracranial and on extracranial metastases in several clinical trials including melanoma and lung cancer patients (2–8). Although variability of the responses is broad and not all patients benefit from it, the use of ICB to treat brain metastasis is widespread. However, many questions remain such as whether or not the therapeutic antibodies do get access to the brain or instead play their role extracranially and then activated T cells infiltrate the CNS (1,9–11). Even more interesting is that, almost all clinical trials have been developed on asymptomatic brain metastases. Thus, the symptomatic state, which is the clinically relevant one, remains poorly studied in the context of immunotherapy. Interestingly, in the limited reports where ICB has been tested on symptomatic brain metastases the therapeutic response rate dropped dramatically (2,7). Although the reason behind the differential response of brain metastases to ICB is unknown, several reasons have been put forward. One of the main explanations is the use of corticoids in symptomatic brain metastasis as the cornerstone strategy to control edema. As a potent immunosuppressor corticoids have been suggested to impair the effect of ICB, however available preclinical data and metanalysis of clinical trials cannot assign the full responsibility to this drug (12–14).

The colonization of the brain by metastatic cells involves changes in the microenvironment. Initially, metastatic cells face a reactive glial response eliminating many of the cancer cells that completed extravasation (15). Subsequently, as the surviving cancer cells resume their growth, they start modifying the environment. As such, altered molecular patterns emerge *de novo* in specific cellular components of the brain. STAT3 is activated in a subpopulation of reactive astrocytes only in advanced stages of the disease when the metastasis has reached a certain size (16). This disease-associated altered molecular pattern contributes significantly to maintain the viability of the metastasis by protecting cancer cells (16). Remarkably, this dependency on a component of the microenvironment was translated into a novel therapeutic opportunity validated in patients (16), which is now in clinical trials (NCT05689619).

Here we report for the first time an unbiased approach to dissect the heterogeneity within metastasis-associated reactive astrocytes at the single cell level. We uncover various populations with distinct gene expression signatures suggesting previously unappreciated complexity at the functional level. Given the immediate clinical implications, we functionally dissected an immunomodulatory program present in a subpopulation within previously identified as STAT3^{+} reactive astrocytes(16) acting on CD8^{+} T cells. We exploit this finding to favor the efficacy of ICB in patients with brain metastases and propose a novel combined immunotherapy compatible with advanced stages of the disease and agnostic to the primary source of the metastasis. The core finding of the novel immunosuppressive mechanism demonstrated in relevant pre-clinical models and in patient-derived samples involves astrocyte derived TIMP1 binding to the CD63 receptor on CD8^{+} T cells, which blocks their activated state. The validation of this phenotype using genetic and pharmacologic approaches allowed us to rationalize a novel combination

4

159 immunotherapy to target local immunosuppression in the brain thus, favoring
160 complementary efforts to activate T cells systemically. Such strategy is
161 complemented with the detection of TIMP1 in liquid biopsy to stratify those patients
162 who could benefit the most from the combined immunotherapy.
163 In summary, our data not only uncover the unexplored role of reactive astrocytes as
164 modulators of T cell function in brain tumors by dissecting disease-associated glial
165 heterogeneity, but also exploit its functional implication on modulating brain
166 infiltrating T cells. We report the potential of developing organ-specific
167 immunotherapies by dissecting the emerging crosstalk between two previously
168 unconnected cell types in the tumor microenvironment.

5

169 **Results**
170
171 **Clusters of brain metastasis-associated reactive astrocytes suggest functional**
172 **diversity including immune-modulation.**
173 As previously reported by us and others(16–20) brain metastasis-associated
174 astrocytes are heterogeneous. However, an unbiased approach to characterize this
175 glial cell type in this pathological context was lacking. We applied scRNAseq on
176 melanoma brain metastasis generated by B16/F10-BrM(16) and enriched the
177 resident glial population by ACSA2 (Fig1A), an established marker for
178 astrocytes(21). Our approach efficiently enriched astrocytes in the single cell
179 population (FigS1A-B) in a non-exclusive way since we detected other cell types
180 post-sequencing (FigS1C). 7762 ACSA2+ astrocytes were profiled to identify 9
181 clusters (Fig1B, SuppTable1), 3 of them (clusters 3, 7 and 6) increased in the
182 presence of brain metastasis (FigS1D, SuppTable2-3). Interestingly, cluster 3 and
183 cluster 7 represent a previously described subpopulation of brain metastasis-
184 associated astrocytes characterized by enrichment in STAT3 expression and
185 activation(16) (Fig1B-C, FigS1E-F). Given the enlarged complexity within the
186 STAT3+ subpopulation, we dissected these two clusters attending to their pathway
187 enrichment. Interestingly, STAT3+ cluster 3 and STAT3+ cluster 7 astrocytes seem to
188 represent functionally different subtypes with non-overlapping top enriched pathways
189 (Fig1D-E, FigS1G, SuppTable4). When analyzing cluster 6, corresponding to a
190 STAT3- brain metastasis-enriched astrocytes cluster, the absence of STAT3+ identity
191 pathways (i.e., interferon-antigen presentation, extracellular matrix and
192 cytokine/integrin signaling) was confirmed (FigS1H, SuppTable4). The functional
193 diversity in STAT3+ clusters could be explained by the different pattern of receptors
194 that activate STAT3, present in these subpopulations of reactive astrocytes. While
195 cluster 3 presents the highest expression of Il6r (FigS1I-K), cluster 7 expresses
196 growth factor receptors that are absent in cluster 3 (FigS1I-J, FigS1L). Additionally,
197 the expression of interaction pairs between cluster 3 and 7 suggests a dynamic
198 evolution of STAT3+ clusters that could potentially modulate each other (FigS1M,
199 SuppTable5). STAT3+ astrocyte clusters (with high *STAT3* expression and activation
200 of STAT3 pathways) were further demonstrated in human brain metastases by
201 scRNAseq (Fig1F-I, FigS1M-O, FigS1P, SuppTable6, SuppTable7). Human STAT3+
202 brain metastasis-associated reactive astrocytes present an increased heterogeneity
203 with a diverse set of functions that include those found in mice clusters (SuppTable8,
204 SuppTable9, SuppTable10). Thus, our findings suggest that STAT3+ clusters include
205 a previously described pro-tumoral component of astrocytes(22) (cluster 3 in mice
206 and 4 in human are enriched in interferon (Fig1D, Fig1I, SuppTable2, SuppTable4,
207 SuppTable8)), but also an unexplored compartment (cluster 7 in mice and cluster 5
208 in human are enriched in extracellular matrix, cytokines and interleukins (Fig1E,
209 Fig1I, SuppTable3, SuppTable4, SuppTable9)).
210 Given that the link between STAT3+ astrocytes and the immune system we
211 previously suggested(16) was reinforced through the dissection of this astrocyte
212 subpopulation at the single cell level with the identification of various
213 immunomodulatory molecules, we decided to functionally test this possibility. We
214 confirmed the immunosuppressive nature of the secretome from pSTAT3+ astrocytes
215 by interrogating CD8+ T cells *in vitro*(16) at the molecular level when incubated with
216 the astrocyte conditioned media (Fig2A-B, FigS2A, SuppTable11). To confirm this
217 finding *in vivo* we evaluated whether CD8+ T cells associated with brain metastasis
218 were dependent on the presence and activity of STAT3+ astrocytes using the STAT3

6

219 inhibitor silibinin(16,23). Although other cell types could be affected by silibinin, the
220 levels of pSTAT3 observed in astrocytes are much higher than in CD8+ T cells(16)
221 (FigS2B), which could suggest an increased functional dependency on this pathway.
222 Addionally, we previoulsy demonstrated that genetically engineering STAT3 loss of
223 function in astrocytes phenocopied the pharmacological intervention(16). With this
224 limitation in mind, we profiled the B16/F10-BrM brain metastasis-associated immune
225 compartment, which includes CD8+ T cells (FigS2C-D) among other cell types
226 (FigS2E), from mice treated with silibinin (Fig2C). Our findings demonstrate that
227 pharmacological blockade of STAT3 alters specifically the proportion of T cell
228 subpopulations in the brain, increasing those clusters expressing known cytotoxic
229 markers (*Cxcr6, Gzmk, Gzma, Gzmb, Ccl5, Gimap7, Xcl1, Klrc1, Klrk1* and *Cd160*),
230 which are not found upregulated in the naïve T cells cluster (Fig2D, FigS2F,
231 FigS2G). In order to evaluate the lack of cell type specificity of the pharmacological
232 intervention, we validated the STAT3-dependent modulation of tumor infiltrating
233 lymphocytes (TILs) using STAT3 depleted mice in reactive astrocytes (GFAP-
234 Cre^{ERT2}; Stat3$^{loxP/loxP}$, abbreviated as cKO^{GFAP}-*Stat3*) (16) (Fig2E). We observed a
235 general increase of brain metastasis associated-CD8+ T cells (FigS2H-I)
236 accompanied with the induction of Granzyme b (Fig 2F-G), which was in agreement
237 with the strong increased of granzyme genes *Gzmb* and *Gzmk* (FigS2J-K). However,
238 no significant alteration in Perforin and IFN-γ expressing CD8+ T cells was observed
239 (FigS2L-M). Thus, inhibition of STAT3, using either pharmacologic or genetic
240 interventions, in brain metastasis-associated reactive astrocytes modulates the
241 phenotype of CD8+ T cells *in vivo*. In order to demonstrate the functional relevance
242 of this finding, we evaluated the ability of a CD8 blocking antibody to rescue the
243 reduced brain metastases burden in cKO^{GFAP}-*Stat3* (Fig2H). Remarkably, blocking
244 CD8+ T cells in cKO^{GFAP}-*Stat3* mice reverted the anti-metastasis phenotype
245 suggesting that the infiltrating immune population is actively suppressed by STAT3+
246 astrocytes *in vivo* (Fig2I-J, FigS2N).
247
248 **TIMP1 and STAT3 in reactive astrocytes correlate with a high immune cluster**
249 **classifier in human brain metastases.**
250 Within the secretome of pSTAT3+ astrospheres(16) several candidates were
251 previously suggested to play a role on the immunosuppressive properties of this glial
252 cell subpopulation(16). Among them, we became particularly interested on TIMP1
253 because it was recently reported as one of the top deregulated proteins within the
254 CD45- cell fraction of human brain metastases, which includes astrocytes(24). Our
255 proteomics data(16) show high TIMP1-specific enrichment in pSTAT3+ astrospheres
256 (FigS3A). We further prove that TIMP1 derives from the microenvironment in human
257 brain metastases (FigS3B-C) and that its highest expression in available scRNAseq
258 data from experimental brain metastases (FigS1C) corresponds to astrocytes when
259 compared to other glial cells or macrophages (FigS3D). Indeed, *Timp1* expression
260 co-localizes with pSTAT3+ astrocytes in astrospheres and in experimental brain
261 metastasis (Fig3A), in particular with STAT3+ cluster 7 (FigS3E, SuppTable3).
262 Furthermore, we confirmed that the major source of TIMP1 in human brain
263 metastases are pSTAT3+ reactive astrocytes (Fig3A, FigS3F-I), where *TIMP1*
264 highest expression is found in the cluster of astrocytes with greatest induction of
265 STAT3 (cluster 5, FigS3J). To demonstrate the contribution of astrocytes to
266 microenvironment-derived TIMP1, we used the genetically modified mouse model
267 (GEMM) GFAP-Cre; Timp1loxP/loxP (for brevity, cKO^{GFAP}-*Timp1*) (25) (FigS3K-Q).
268 We validated the absence of TIMP1 in the conditioned medium of pSTAT3+

7

269 astrospheres[16] derived from cKO^GFAP-*Timp1* GEMM (FigS3O-P), where we were
270 unable to detect any influence of TIMP1 on the established phenotype of this *in vitro*
271 surrogate for pSTAT3+ astrocytes[16] (FigS3N). Accordingly, GFAP+ pSTAT3+ brain
272 metastasis associated-reactive astrocytes in cKO^GFAP-*Timp1* GEMM remain
273 indistinguisable from wild type ones (FigS3K-M). No additional analyses were
274 performed to characterize astrocytes in the cKO^GFAP-*Timp1* GEMM. Importantly,
275 depleting *Timp1* from astrocytes decreases brain metastasis-induced TIMP1 to non-
276 tumor levels in the cerebrospinal fluid (CSF) (FigS3Q). Finally, we confirmed the
277 STAT3-dependency of TIMP1 *in vivo* with both cKO^GFAP-*Stat3* mice (FigS3O) and
278 pharmacological inhibition of STAT3 (FigS3R-T).
279 As we hypothesized that STAT3+ astrocytes are major contributors to local
280 immunosuppression, we asked whether this astrocyte population correlated with the
281 degree of immune infiltration in the microenvironment of human brain metastases.
282 We interrogated the expression of *STAT3* and *TIMP1* in patient samples previously
283 profiled with transcriptomics and annotated respect to low, medium and high immune
284 categories[26] (Fig3B, FigS4A). Remarkably, both *STAT3* and *TIMP1* expression
285 levels were enriched among human brain metastases classified as the high immune
286 fraction (Fig3C-D). Of note, scored samples were compatible with reporting gene
287 expression patterns from the microenvironment compartment (FigS4B). The
288 correlation between the genes of interest and the immune compartment was
289 validated in a second cohort of human brain metastases (FigS4C-D, SuppTable12).
290 This finding could suggest that the expression of *STAT3* and *TIMP1* genes is
291 compatible with a dense immune landscape broadly speaking, which could
292 potentially involve the ability of these fraction of brain metastases to respond to
293 immune checkpoint inhibitors if properly stimulated. Interestingly, we realized that the
294 definition of human samples according to the different immune categories was
295 reproduced by a reduced gene classifier composed by genes representative of key
296 cell types from the microenvironment including *CD8a* (for CD8+ T cells and some
297 subsets of dendritic cells), *CD68* (for microglia/macrophages) and *ITGAX* (mainly for
298 dendritic cells, but also for macrophages, NK cells and granulocytes) (Fig3B and
299 FigS4E-F). The use of these reduced number of markers to assess the immune
300 infiltration of human brain metastasis could provide a clinically-compatible assay that
301 might be useful to stratify patients. Consequently, we develop a multiplex analysis
302 applying the corresponding antibodies for these cell types to a cohort of 12 selected
303 brain metastases in RENACER[27] (List of supplementary figure, supplementary
304 tables and authors included in the RENACER signature). The selection criteria
305 applied responded to the inclusion of samples obtained through extended
306 neurosurgical resection (Fig3E, SuppTable13) to make sure a substantial peritumoral
307 microenvironment, where astrocytes are exclusively located, was present (Fig3E)
308 [15]. Samples were categorized into low/ medium/ high based on the combined
309 score of the three antibodies (Fig3F, FigS4G), which nicely correlated with the
310 transcriptomic scoring (Fig3G). Analysis of the abundance of *TIMP1* in the
311 microenvironment of these samples confirmed the correlation with the high immune
312 cluster (Fig3G). Based on these findings, we hypothesized that patients with brain
313 metastasis treated with immune checkpoint blocking antibodies, even in the
314 presence of an immune rich microenvironment, might not benefit from this
315 immunotherapy given the concomitant presence of a local immunosuppressive
316 compartment (i.e., pSTAT3+ astrocytes). Although an adequate comparison with the
317 responders is a requisite, to preliminary evaluate our hypothesis, we identified in
318 RENACER 8 patients affected with extracranial metastases that responded to

8

319　immune checkpoint blockade systemically but that later relapsed in the brain (Fig3H,
320　SuppTable14). Our ability to get access to these tissues from the RENACER
321　cohort(27) allowed us to confirm the presence of pSTAT3+ reactive astrocytes
322　enriched in *TIMP1* (Fig3H). As CD8+ T cells are present in limited numbers
323　infiltrating the tumor core, but mainly in the peritumoral area intermingled with
324　reactive astrocytes (FigS4H), we hypothesized that a correlation between the
325　potential anti-tumor quality of CD8+ T cells and the distance to pSTAT3+ reactive
326　astrocytes might exist. Interestingly, we found that this cohort of patients shows an
327　inverse correlation between the density of pSTAT3+GFAP+ cells and granzyme
328　positive CD8+ T cells (Fig3I-J), by focusing on areas within the range of influence of
329　cytokines(28). Thus, our findings provide the rationale to improve responses to
330　immune checkpoint blockade in brain metastases with high immune infiltration by
331　targeting STAT3+ astrocyte-dependent local immunosuppression.
332
333　**TIMP1 mediates brain metastasis in a CD8+ T cell-dependent manner**
334　To address the potential contribution of astrocyte-derived TIMP1 to the
335　immunosuppressive phenotype on CD8+ T cells (Fig2A-J) we performed *in vitro*
336　cytotoxicity assays. CD8+ T cell cytotoxicity was analyzed using OT-I transgenic
337　CD8+ T cells specific for the OVA-derived SIINFEKL peptide(29) and targeted
338　B16/F10-BrM-OVA^{GFP} cells (Fig4A, FigS5A-B). As previously reported, activated
339　CD8+ T cells cultured in the secretome of pSTAT3+ astrospheres reduced their
340　cytotoxicity compared to pSTAT3- secretome addition, on a melanoma brain
341　metastatic cell line(16) (Fig4B, FigS5C-D). We found that addition of TIMP1 mimics
342　the effect of the immunosuppressive pSTAT3+ secretome (Fig4B, FigS5C-D), in the
343　same line as described by Oelmann et al(30). In addition, pSTAT3+ astrospheres
344　generated from cKO^{GFAP}-*Timp1* were unable to influence the cytotoxicity of activated
345　T cells (Fig4B, FigS5C-D). These results were complemented with *in vitro*
346　experiments with activated T cells, where anti-TIMP1 blocking antibody reverted the
347　effect of the otherwise immunosuppressive pSTAT3+ secretome (FigS5E-G). In
348　order to expand this finding to more relevant models we applied the blocking
349　antibody against TIMP1 to organotypic cultures of both experimental (Fig4C) and
350　patient-derived brain metastases *ex vivo* (Fig4D, SuppTable15) that included the
351　surrounding microenvironment where astrocytes and T cells co-exist (FigS5H-I)
352　(16). Remarkably, blocking TIMP1 activity correlated with reduced metastasis-
353　derived bioluminescence that was rescued by blocking CD8+ T cells (Fig4E).
354　Targeting human TIMP1 in eleven patient-derived brain metastasis organotypic
355　cultures (PDOC) from different primary tumors confirmed the decrease viability of
356　metastases (Fig4F). We further demonstrate that the phenotype was not direct on
357　cancer cells since anti-TIMP1 blocking antibody did not significantly influence
358　metastatic cells in isolation (FigS5J-L). Consistent with the mouse model, the
359　reduction in the viability of human brain metastatic cells was rescued by targeting the
360　CD8+ T cells infiltrating the PDOC in an additional cohort of seven patients (Fig4G).
361　Remarkably, patients stratified as high immune cluster (FigS5M, SuppTable16),
362　which we hypothesized to respond better to anti-TIMP1 blockade in PDOCs, showed
363　a greater decrease in cancer cell viability compared to patients with limited CD8+ T
364　cell infiltration, low levels of STAT3 and TIMP1 and similar levels of dendritic cells
365　and macrophages markers (FigS5N, SuppTable16). To expand the involvement of
366　TIMP1 *in vivo* we performed metastasis assays with two experimental models. A
367　melanoma brain metastasis model(16) and a triple negative breast cancer (TNBC)
368　model(31) were inoculated in the cKO^{GFAP}-*Timp1* GEMM(25) (Fig4H). Brains with

9

369   conditional knock-out of *Timp1* in reactive astrocytes correlated with a decreased
370   ability of metastatic cells to survive in this organ (Fig4I-L, Fig5SO-P). Analysis of the
371   histology showed increased numbers of anti-tumoral brain metastasis-associated
372   CD8+ T cells infiltrating the metastasis (Fig4M-N), which strongly suggest a potential
373   negative influence of resident glial cells on the acquired immune system at the core
374   of local immunosuppression.
375
376   **Characterization of the influence of TIMP1 in CD8+ T cells**
377   We characterized the influence of STAT3/TIMP1 on CD8+ T cells using
378   immunophenotyping with different coactivatory, coinhibitory markers and cytokines.
379   Flow cytometry analysis confirmed that, according to the decrease in cytotoxicity we
380   observed previously (Fig4B, FigS5C-D, FigS5E-G), pSTAT3+ conditioned media
381   (CM) decreased expression of CD25 in effector CD8+ T cells (Fig5A, Fig5B-C).
382   Furthermore, CD25 downregulation was rescued upon depletion of *Timp1* in
383   astrocytes (Fig5B-C). Absence of TIMP1 downstream STAT3 leads to increase of
384   CD8+ T cells expressing inflammatory cytokines (Fig5A, Fig5D) and a decrease in
385   exhausted CD8+ T cells (Fig5A, Fig5E). Furthermore, brain metastasis-associated
386   CD8+ T cells increased CD44 and INFγ levels, while reduced exhaustion markers
387   when TIMP1 was depleted from reactive astrocytes *in vivo* (Fig5F, Fig5G-L). TIMP1
388   has been mostly studied as a regulator of MMPs(32), however its role as a ligand
389   binding to CD63 receptor(33) has not been addressed until recently(32,34,35). We
390   tested if TIMP1 pro-tumoral role in brain metastasis depends on its interaction with
391   MMPs or on its cytokine activity in organotypic cultures. Only blocking TIMP1 regions
392   non-interacting with MMPs leads to a decrease in brain metastasis (FigS6A-C).
393   CD63 has been previously suggested as a marker of CD8+ T cell activation(36),
394   which we reproduced *in vitro* (FigS6D). Although, we detected a trend towards an
395   increased percentage of circulating CD8+ T cells expressing CD63 when there is
396   systemic disease in preclinical models (FigS6E), a robust and significant increase in
397   the surface levels of CD63 was only detected when the CD8+ T cell fraction was
398   evaluated in established brain metastases (Fig6A, Fig6B-D, FigS6F-G) (24).
399   Furthermore, we confirmed the presence of CD63+CD8+ T cells *in situ* in both
400   experimental and patient-derived brain metastases (Fig6C-D). We probed the
401   binding of astrocyte-derived TIMP1 and CD63 on the surface of CD8+ T cells in co-
402   cultures of pSTAT3+ astrospheres and *in vitro* activated CD8+ T cells, while the
403   culture of these two cell types independently of each other did not reproduce the
404   binding if the two molecules (Fig6E, FigS6H). This finding was further validated *in
405   situ* in human brain metastasis samples, detecting specific signal in proximity ligation
406   assays (Fig6F, FigS6I). The fact that the level of CD63 receptor increases along with
407   the activation state of CD8+ T cells (FigS6D) and that the binding of its ligand,
408   TIMP1, triggers an immunosuppressive phenotype (Fig4B, Fig5A-E, Fig5G-L) might
409   be suggestive of a potential paracrine immune checkpoint. To consolidate this
410   hypothesis, we first evaluated whether CD8+ T cells from CD63-null mice(37) exhibit
411   improved anti-tumor ability (Fig6G). Addition of wild type CD8+ T cells to organotypic
412   cultures of established brain metastases generated with the B16/F10-BrM cell line
413   was not sufficient to reduce significantly the viability of cancer cells (Fig6H), which
414   reinforces the influence of the immunosuppressive microenvironment. In contrast,
415   the absence of CD63-TIMP1 signaling when CD63 KO CD8+ T cells were added to
416   organotypic cultures, allowed an effective T cell-mediated killing of cancer cells
417   (Fig6H). To further confirm the differential impact of TIMP1 among CD63^{low} and
418   CD63^{high} CD8+ T cells, sorted CD8+ T cells with low or high CD63 levels were

10

419 treated with CM from either wild type or cKO^{GFAP}-*Timp1* pSTAT3+ astrospheres
420 (FigS6J-N). While CD8+/CD63^{low} T cells did not respond to the presence of TIMP1
421 from STAT3+ astrospheres CM, CD8+/CD63^{high} T cells increased CD44/ CD62L
422 levels when TIMP1 was not present (FigS6L-N). Additionally, cytotoxicity genes
423 *Gzmb* and *Gzmk* were induced in sorted brain metastasis associated-CD8+/CD63^{high}
424 T cells when *Timp1* was depleted from reactive astrocytes (Fig6I, FigS6O). Our
425 findings report a novel molecular crosstalk between STAT3+ reactive astrocytes and
426 CD8+ T cells through TIMP1-CD63 leading to the decrease of the anti-tumor activity
427 of this component of the acquired immune system infiltrating the brain. However, due
428 to the lack of knowledge on the signaling pathways downstream of CD63 in
429 lymphocytes upon TIMP1 binding we performed phosphoproteomics analysis to
430 deepen our findings on T cell immunosuppression in brain metastasis. *In vitro*
431 activated CD8+ T cells were analyzed by LC-MSMS-based proteomics after
432 incubation with CM from pSTAT3+ astrospheres derived from wild type or cKO^{GFAP}-
433 *Timp1* astrocytes (Fig6J, FigS7A). Lack of TIMP1 signaling on CD8+ T cells lead to a
434 main enrichment of signatures related to T cell activation as the top finding (FigS7B,
435 SuppTable17). Dissecting the phosphosites significantly altered when the
436 immunosuppressive signal activated by TIMP1 was not present revealed several
437 kinases with altered levels of their phosphorylated substrates (Fig6K, SuppTable18).
438 Among them, we validated changes in ERK1/2 phosphorylation (pERK1/2) in CD8+
439 T cells infiltrating metastases when targeting TIMP1 in astrocytes (cKO^{GFAP}-*Timp1*)
440 (Fig6L, FigS7C). Furthermore, analysis of human brain metastases scored with
441 multiplex (Fig3E-G) showed a correlation between the quality of infiltrating CD8+ T
442 cells regarding their pERK1/2 status and their immune cluster category (Fig6M,
443 FigS7D, SuppTable19). Finally, we validated the modulation of ERK activity using
444 rTIMP1 or anti-TIMP1 on CD8+ T cells while incubated in astrospheres conditioned
445 medium (FigS7E). Overall, we report that signaling downstream of CD63 receptor
446 has major implications in anti-tumor activity of CD8+ T cells upon TIMP1 binding
447 through the modulation of multiple kinases including ERK1/2 (Fig6N).
448
449 **A combined immunotherapy targeting local immunosuppression provides**
450 **superior control of brain metastasis.**
451 In order to demonstrate the therapeutic implications of our findings we decided to
452 test whether inhibition of STAT3 could be combined with immune checkpoint
453 blockade (ICB) to obtain better anti-tumor responses in the brain (Fig7A). The
454 B16/F10-BrM model responded to anti-PD1/ anti-CTLA4 extracranially (Fig7B,
455 FigS8A) but did not decrease tumor burden in the brain (Fig7B, FigS8B).
456 Complementary, as previously reported(16), the STAT3 inhibitor silibinin achieved a
457 significant control of brain metastases (Fig7B, FigS8B) but with limited extracranial
458 benefit (Fig7B, FigS8A). Although brain bioluminescence imaging (BLI) *ex vivo* did
459 not show any additional benefit of the ICB and silibinin combination beyond the
460 response to silibinin monotherapy (FigS8B), histological examination of these brains
461 demonstrated that the response was clearly superior (Fig7C, SuppTable20).
462 Interestingly, although large metastases were mainly controlled by silibinin,
463 metastases of medium size were more effectively targeted by ICB with the
464 combination therapy (Fig7C, SuppTable20). The apparent dissociation between BLI
465 and histology might suggest that the data obtained with bioluminescence is mainly
466 contributed by large lesions, thus lacking the sensitivity to score changes affecting
467 metastases from other size categories. In fact, we previously reported that silibinin
468 was not effective against smaller metastasis both in experimental models and

patients since STAT3+ reactive astrocytes are not present(16). We hypothesized that the combined immunotherapy including silibinin could sensitize experimental metastases to the attack of CD8+ T cells activated systemically with ICB. Accordingly, we evaluated whether the anti-tumor response was increased when targeting local immunosuppression with silibinin in the brains of ICB treated mice. Histological analysis of the brains from mice treated with the combined immunotherapy showed increased markers of cytotoxic activity (Fig7D-E) and cleaved caspase 3-staining in cancer cells (FigsS8C-D). In order to reinforce our finding, to discard any influence of extracranial metastasis in the brain phenotype(11) and to explore the potential additional benefit of a combination with radiotherapy, we repeated the combination therapy using intracranial injection in this model to apply local therapy (Fig7F), as previously reported(31). Since the B16/F10-BrM model lacks a recently described radioresistance mechanism(31), we found it does respond to fractionated radiotherapy (FigS8E). Accordingly, we added ICB and silibinin to irradiated mice and scored whether any additional benefit in overall survival was detected beyond what is provided by the local therapy. In this experimental setting, ICB showed a superior ability to target brain metastases mimicking the effect of silibinin (FigS8F). More importantly, the triple combination therapy did add additional brain tumor control increasing overall survival (Fig7G, FigS8F). Consistently, the combined immunotherapy led to a more efficient cancer cell killing (Fig7H-I) and more proliferative CD8+ T cells locally (Fig7J-K). To expand our finding to other relevant preclinical models and test whether the improved control of brain metastasis when combining ICB and STAT3 inhibition was triggered by impairing TIMP1-mediated immunosuppression, we used the cKO^{GFAP}-*Timp1* mice intracardially injected with E0771-BrM cells and treated with ICB (FigS8G). We found that abolished secretion of the STAT3 downstream target TIMP1 in reactive astrocytes improved ICB benefit in brain metastasis (FigS8H-J), affecting both metastases of medium and big size (FigS8K-L, SuppTable20).

Our initial findings suggest the feasibility of using TIMP1 to stratify patients that could benefit from the combined immunotherapy (Fig3D). However, a systemic treatment should not rely on a biomarker requiring neurosurgery to score tissue samples. Consequently, given the secretory ability of STAT3+ RA(16), which includes TIMP1 (FigS3A), together with existing reports using astrocyte-derived biomarkers in liquid biopsies(38,39), we evaluated such possibility in patients with brain metastasis. The cerebrospinal fluid (CSF) has been suggested as a better surrogate to the brain parenchyma than blood(40–43), so we decided to evaluate TIMP1 in these two types of liquid biopsies from the RENACER cohort. While TIMP1 levels in the blood did not differ from healthy controls individuals (FigS9A, SuppTable21), the CSF from patients with brain metastasis was significantly enriched in the potential biomarker (Fig7L, SuppTable21). Furthermore, high levels of TIMP1 in CSF of brain metastasis patients predicts worse overall survival (FigS9B, SuppTable22). In order to evaluate the correlation between the biomarker and the susceptibility to respond to strategies that block local immunosuppression, we checked whether any of these patients also had PDOC established from extended neurosurgeries as part of the RENACER pipeline(27). A selected group of samples with confirmed presence of immune cells compatible with medium-high immune clusters (Fig3G, FigS9C-D, SuppTable21, SuppTable23-25) with PDOC and values of TIMP1 in the CSF above the mean of healthy controls could be allocated. According to the data reported above, PDOC proved their sensitivity to the blocking anti-TIMP1 antibody (Fig4F, Fig7M, Fig7N, FigS9C, SuppTable15, SuppTable21) in a CD8+ T cell dependent manner (Fig4G).

519 Thus, our data provides the rationale to test a novel combined immunotherapy
520 consisting on ICB antibodies and silibinin as a strategy to maximize the access to
521 metastases and anti-tumor activity of CD8+ T cells by blocking local
522 immunosuppression. In addition, the therapeutic strategy described could potentially
523 be guided by a biomarker compatible with liquid biopsy to improve patient
524 stratification and evaluation of the therapeutic benefit. Overall, our finding represents
525 the first comprehensive approach to target symptomatic brain metastases with a
526 biomarker-guided immunotherapy.
527
528 **Discussion**
529 Recent clinical trials have tested ICB antibodies in patients with brain metastasis
530 derived from melanoma and lung cancer(2–8). The results indicate variable rates of
531 positive responses that could oscillate between 0-60% of the patients. However,
532 positive response rates were mainly attributable to asymptomatic brain metastasis,
533 which tend to be smaller in size. Indeed, in those trials where symptomatic brain
534 metastases were considered, ICB benefits for intracranial lesions dropped
535 significantly(2,7), which has created concerns regarding their translation to real world
536 clinical practice(44). Although corticoids have been suggested to underlie this
537 differential responses among patients it remains controversial(7,12–14,45).
538 The data reported here could potentially explain these clinical findings to some
539 extent since our previous observations concluded that pSTAT3+ reactive astrocytes
540 are not present in early but in advanced stages of the disease(16) and patients
541 treated with silibinin, a STAT3 inhibitor(16,23), decreased the size of the metastasis
542 to a certain point, which then remain stable(16). Thus, we conclude that the lack of
543 local benefit from ICB in patients with symptomatic brain metastasis reflects, rather
544 or in addition to a potential consequence of the use of corticoids, a pSTAT3+ reactive
545 astrocytes-driven mechanism that is responsible for local immunosuppression
546 affecting CD8+ T cells arriving from the periphery. Thus, although ICB might facilitate
547 the access of active T cells into the brain, these potential cellular anti-tumor entities
548 suffer the local immunosuppressive environment that might underlie the requirement
549 of a combination therapy.
550 Our data indicates that, the presence of brain metastasis alters the immune
551 landscape in the brain increasing immune cells numbers, however brain metastasis-
552 associated T cells remain ineffective to target cancer cells. By dissecting astrocyte
553 heterogeneity, we found subpopulations of astrocytes enriched in potential
554 immunomodulatory signatures. When exploring the molecular basis of
555 immunomodulation mediated by metastasis-associated astrocytes, we found that the
556 STAT3-dependent gene *TIMP1*, previously reported as a top differentially expressed
557 protein in human brain metastasis samples(24), imposes a local immunosuppressive
558 hub affecting the quality of CD8+ T cells. We demonstrate that the main source of
559 TIMP1 is in the tumor microenvironment, and specifically a subpopulation of reactive
560 astrocytes. TIMP1 has been mostly considered an MMP inhibitor(32). However,
561 TIMP1 also plays an MMP-independent role by binding to CD63(32–35,46). We
562 report a novel function for TIMP1/CD63 on the surface of CD8+ T cells infiltrating
563 brain metastasis mediating immunosuppression in an antigen dependent and
564 independent manner. Although the acquired immune system is necessary for
565 STAT3/TIMP1-mediated immunosuppression, considering the non-restricted
566 expression of CD63 on CD8+ T cells, it could be presumed that extracellular vesicles
567 expressing CD63 and other cell types such as macrophages, may be also affected
568 by TIMP1 increased in the brain metastasis microenvironment. The potential

569 involvement of this and other immune cell types including dendritic cells that are also
570 directly affected by STAT3 inhibition in reactive astrocytes or as a consequence of
571 the improved immune landscape, should be further addressed. Additionally, although
572 our genetic strategy confirmed that STAT3 inhibition with silibinin is recapitulated with
573 an astrocyte-specific targeting approach on STAT3; we cannot fully discard that the
574 pharmacological strategy is also affecting other cell types. Whether the
575 immunosuppressive role of the reactive astrocyte subpopulation could play a role in
576 other brain disorders remains to be addressed. Indeed, it is tempting to speculate
577 that given the role of astrocytes to limit potential threats to the brain, this could
578 include their ability to block infiltrating T cells, which might otherwise increase the
579 risk of causing deleterious consequences in this low regenerative organ.
580 Given that silibinin targets pSTAT3+ reactive astrocytes(16) we propose that the
581 combination with ICB will increase local responses by facilitating CD8+ T cell anti-
582 tumor activity in patients with brain metastasis. It should be noted that, silibinin could
583 be affecting systemic T cells and its effects may be potentiated by the action of
584 radiotherapy-promoted T cell priming(47). Even more, the fact that the levels of
585 STAT3 and TIMP1 are enriched in those patients where the local environment is
586 compatible with a potential response to ICB (i.e., high immune cluster) justifies the
587 use of TIMP1 as a potential biomarker. CSF liquid biopsy to detect TIMP1 would
588 allow not only selecting the patients who would benefit the most from the combined
589 immunotherapy, but also to follow the therapeutic response over time.
590 Overall, our study demonstrates that dissecting the heterogeneity within the
591 metastasis-associated microenvironment to cell type specific subpopulations defined
592 functionally (i.e., mouse cluster 7 and human cluster 5 within STAT3+ reactive
593 astrocytes) offers the possibility to develop novel therapeutic vulnerabilities. By
594 exploring a specific crosstalk within the altered brain metastasis microenvironment
595 (TIMP1 ligand binding to CD63 receptor) we might have contributed to clarify an
596 unsolved clinical limitation (i.e., lack of response in symptomatic brain metastases).
597 Given the preliminary data that we show in patients, the rationale of combining
598 silibinin with ICB as a more effective immunotherapy for brain metastases supports a
599 follow-up clinical trial after completing the one currently ongoing with silibinin as
600 monotherapy (NCT05689619).
601

Acknowledgments

635   **Author contributions**
636   N.P.: Conceptualization; Data curation; Formal analysis; Validation; Investigation;
637   Visualization; Methodology; Writing-original draft; Writing-review and editing. A.P-A.,
638   M.P-G., V.P., L.A-E., A.R., O.S., D.S., B.J-L., L.E-M.: Formal analysis; Investigation;
639   Visualization; Methodology. C.H-O., S.G-M., O.G-C.: Data curation; Formal analysis;
640   Methodology. P.V-B.: Data curation; Formal analysis; Investigation; Methodology.
641   L.R.,A.S.: Data curation; Formal analysis; Investigation; Visualization; Methodology.
642   E.C.: Formal analysis; Supervision; Visualization; Methodology. F.G.: Data curation;
643   Formal analysis; Investigation; Methodology. A.S., S.G-M., R.S-P.: Formal analysis;
644   Supervision; Validation. E.M-S., A.P-N., A.H-L.: Human samples and clinical
645   evaluation. S.J.C.: provided the Timp1loxP/loxP mice. P.S.: provided the CD63-null
646   mice. M.S.,A.C-C.,A.P.: Resources, Formal analysis; Supervision; P.B., V.C., C.S.,
647   D.A., N.A., M-J.A., E.O-P., A.G., C.F., A. de la L., A.L., A.D., P.D., M.P., A.D-P., SH.N-
648   C., C.B., G.P., B.E., I.G., S.A., A.P., A.H., O.T., R.G., JA.F., G.B., L.B., A.P., R.D.,
649   P.C., L.M., R.S., S.C.C., E.M., M.M., M-S-O., A.R., F.M., S.RyC., M.S.F., L.F.:
650   Supervision; provided and processed the human samples and collected clinical data;
651   M.V.: Conceptualization; Resources; Project administration; Formal analysis;
652   Supervision; Funding acquisition; Validation; Investigation; Visualization;
653   Methodology; Writing-original draft; Writing-review and editing.
654

655   **Material and methods**
656   <u>Animal studies</u>
657   All animal experiments are in accordance with a protocol approved by the CNIO,
658   Instituto de Salud Carlos III and Comunidad de Madrid Institutional Animal Care and
659   Use Committee (IACUC.030-2015, CBA35_2015-v2 and PROEX135/19). The
660   cKO^{GFAP}-*Stat3* model was generated by breeding GFAP-CRE/ERT2 (B6.Cg
661   Tg(GFAP-cre/ERT2)505Fmv/J, Jackson Labs, ref. 012849) with STAT3loxP/loxP,
662   cKO^{GFAP}-*Timp1* was generated as described by Sutter et al[25] and CD63-null mice
663   was generated as described by Schröder et al[37]. Tg(TcraTcrb)1100Mjb/J (OT-I
664   mice) were kindly provided by D. Sancho (CNIC) for the isolation of OT-I T cells.
665   Brain colonization assays were performed in 10-15 weeks old mice, both males and
666   females (except for the E0771-BrM cells that were injected in females), as previously
667   described[16] by injecting 100 µl of PBS into the left ventricle containing 100,000
668   cancer cells or 1 µl of PBS intracranially (right frontal cortex, approximately 1.5 mm

15

lateral and 1 mm caudal from bregma, and to a depth of 2 mm) containing 40,000 cancer cells by using a gas-tight Hamilton syringe and a stereotactic apparatus.

Brain colonization was analyzed *in vivo* and *ex vivo* by bioluminescence imaging (BLI). Mice were anesthetized with isofluorane and injected retro-orbitally with D-Luciferin (150 mg/kg) and imaged with IVIS® Spectrum and Lumina III In Vivo Imaging System (Caliper Life Sciences). Bioluminescence analysis was performed using Living Image software, version 64. *Ex vivo* values at the endpoint were normalized to the BLI values of the head *in vivo* three days after injection of the cancer cells before starting treating with the different drugs. Tamoxifen (I.p., 1 mg/day) was administered three days after cancer cells inoculation until the end of the experiment, Silibinin in the formula of Silymarin 77.5% (Euromed, Code No. 345316.00) was administered by oral gavage daily (200 mg/kg) three days after cancer cells inoculation and treatment continued until mice reached the endpoint of the experiment. Starting three days after cancer cells inoculation, Control IgG (i.p; 10 mg per kg, BioXcell, ref. BE0090), Anti-CD8α (i.p; 10 mg per kg, BioXcell, ref. BE0061), Anti-PD1 (i.p; 10 mg/ kg BioXcell, ref. BE0146) and Anti-CTLA4 (i.p; 10 mg/ kg, BioXcell, ref. BE0032) antibodies were administrated every two days during the first two weeks of treatment and in non-consecutive days during the last week of treatment.

Radiotherapy

Three days after intracranial injection of B16/F10-BrM cells, the presence of established brain metastases was confirmed by BLI. WBRT protocols mimicking the clinical procedure were applied as previously described(31): fractionated dose of 3 Gy per day for 5 consecutive days or completed regimen with 3 Gy per day for additional 5 days after 2 days without irradiation. Mice were followed up by BLI until the humane endpoint was reached.

Brain slice assays

Organotypic slice cultures from adult mouse brain were prepared as previously described(16). Organotypic cultures included brains obtained at the endpoint of metastatic disease when brain lesions are established. Brains were dissected in Hank's balanced salt solution (HBSS) supplemented with HEPES (pH 7.4, 2.5 mM), D-glucose (30 mM), CaCl2 (1 mM), MgCl2 (1 mM), NaHCO3 (4 mM), and embedded in low-melting agarose (Lonza) preheated at 42° C. The embedded brains were cut into 250 µm slices using a vibratome (Leica). Slices were divided at the hemisphere into two pieces. Brain slices were placed with flat spatulas on top of 0.8 µm pore membranes (Sigma Aldrich) floating on slice culture media (Dulbecco's modified Eagle's medium (DMEM), supplemented HBSS, fetal bovine serum 5%, D-glucose (30 mM), L-glutamine (1 mM), 100 IU/ml penicillin, 100 mg/ml streptomycin). BLI was acquired after generating brain slices (Day 0) to confirm the presence of brain metastasis and 3 days after the addition of the inhibitor (Day 3) considering for analysis floating brain slices. Growth rate was obtained by comparing fold increases between day 3 and day 0. In the case of T cell addition, 20,000 CD8+ T cells were seeded on the top of established brain metastasis brain slices after one day in culture. Control IgG (10 µg/ml, BioXcell, ref. BE0090) or preservative (0.05% Sodium azide) was added in the control condition if necessary, Anti-TIMP1 antibody (102D1) (10 µg/ml, Thermofisher, ref. MS608PABX), Anti-TIMP1 (N-terminal) (10 µg/ml, Sigma Aldrich, ref. SAB2109118), Anti-TIMP1-Carboxyterminal end (10 µg/ml, Abcam, ref. ab38978), and Anti-mouse CD8α (100 µg/ml, BioXcell, ref. BE0061)

16

719 were added to the media at day 0. Brain slices were fixed in paraformaldehyde (4%)
720 overnight followed by free-floating immunofluorescence.
721
722 <u>Cell culture</u>
723 Mouse brain metastatic cell lines have been generated as previously
724 described(16,31). All cell lines were tested negative for Mycoplasma (by qRT-PCR).
725 We did not do cell authentication beyond visual, morphological and growth rate
726 analyses. The maximum number of passages between thawing and use are 15 for
727 all the cell lines.
728 B16/F10-BrM were cultured in DMEM media supplemented with 10% fetal bovine
729 serum (FBS), 2 mM L-Glutamine, 100 IU/ml penicillin/streptomycin and 1 mg/ml
730 amphotericin B, E0771-BrM were cultured in RPMI1640 medium supplemented with
731 10% FBS, 1% HEPES, 2 mM L-glutamine, 100 IU/ml penicillin/streptomycin and
732 1 mg/ml amphotericin B. B16/F10-BrM-OVA^{GFP} cells were generated by lentiviral-
733 mediated transduction of a truncated non-secreted ovalbumin (OVA)-GFP fusion
734 protein (bm1 T OVA) generously supplied by D. Sancho (CNIC). HEK 293T cells
735 (cultured in DMEM media supplemented with 10% FBS, 2 mM L-glutamine, 100
736 IU/ml penicillin/streptomycin and 1 mg/ml amphotericin B) at 70% confluence were
737 transfected in Opti-MEM with Lipofectamine 2000 (Invitrogen) and incubated at 37°C
738 overnight with the corresponding plasmids. Mouse astrocytes were obtained from
739 one to three-day old pups(16). Brains were mechanically dissociated, filtered through
740 70 µm filters and cell suspension was cultured in a petri dish for the next seven days.
741 After gentle shaking at 37 °C overnight, the media was changed.
742
743 <u>Astrosphere assays</u>
744 Astrospheres were generated as previously described(16). Briefly, mouse astrocytes
745 were obtained from mechanical dissociation of brains from 1- to 3-day-old pups. After
746 7 days in culture and gentle shaking overnight at 37 °C, the media was changed and
747 astrocyte enrichment was confirmed. Astrocytes were treated with a cytokine cocktail
748 including EGF (0.01 µg/ml, R&D Systems, ref. 2028-EG-200), MIF (0.1 µg/ml, R&D
749 Systems, ref. 1978-MF-0257CF) and TGFα (0.1 µg/ml, R&D Systems, ref. 239-A-
750 100) in DMEM media with B27 (1x) for 96 hours. After treatment, 5x104 astrocytes
751 were seeded in low attachment plates and incubated for seven days in the presence
752 of the same media to evaluate the ability to form astrospheres. Conditioned media
753 was collected, filtered and added to activated CD8+ T cells.
754
755 <u>Immunoblotting</u>
756 Lysis buffer (Cell Signaling ref. 9803S) with the following protease inhibitors: 200 mM
757 Na3VO4, 500 mM NaF, 100 mM PMSF, was used to extract total protein. Protein
758 lysate from the microenvironment was obtained by dissecting Luciferase- tissue
759 immediately adjacent to Luciferase+ cancer cells. Microdissection was initially
760 validated by confirming the absence of GFP+ cells using flow cytometry. Tissue was
761 mechanically desegregated with the FastPrep-24™ 5G lysis system (MPBiomedical)
762 by using zirconium beads at 6.0 m/s for 15 s followed by 10 min incubation on ice
763 before lysis. For protein quantification, BCA protein color kit was used (Fisher
764 Scientific, ref. 23227). After denaturalization, 10-50 ug of protein lysates were
765 resolved by SDS-PAGE. Transfer to PVDF membranes (VWR, ref. 10600021) was
766 carried out in transfer buffer 1X (Alaos, ref. TT5C-10) 20% methanol for 2 hr 100V.
767 Blocking was performed with 5% milk and membranes were washed with TBS-
768 Tween 0.1 %. The following primary antibodies: p44/42 MAPK (Erk1/2) (1:1000, Cell

17

769 Signaling, ref. 9107), Phospho-p44/42 MAPK (Erk1/2) (1:1000, Cell Signaling, ref.
770 4370), Anti-TIMP1 (1:1000, Thermofisher, ref. MS608PABX), Anti-CD63 (MX-
771 49.129.5) (1:500, Santa Cruz, ref. sc-5275), Anti-Tubulin (1:5000, Santa Cruz, ref.
772 sc-17787), Anti-vinculin (1:10000, Sigma, ref. V9131) and secondary antibodies from
773 Invitrogen (AF680) and LiCor Odissey CLx system were used for visualization.
774
775 Immunoprecipitation
776 For immunoprecipitation, co-cultures of STAT3+ astrospheres (as described above)
777 and CD8+ T cells (cultured *in vitro*) were performed. CD8+ T cells were added over
778 STAT3+ astrospheres (washed with PBS 1X after gently centrifugation) in a
779 concentration of 6x105 CD8+ T cells/1.5 ml of co-culture. After 72 hours in culture,
780 1000 µg of total protein extract was incubated at 4 ºC overnight with Anti-CD63 (MX-
781 49.129.5) (Santa Cruz, ref. sc-5275), or isotype control (IgG1, Cell Signaling, ref.
782 #5415) in a concentration of 10 µg/mg of protein. Dynabeads protein-G
783 (Thermofisher, ref. 10003D) were vortexed and washed twice. Then, 50 µl were
784 incubated with the different fractions for 2 hours at 4 ºC. Finally, samples were
785 washed and eluted for detection of CD63 and TIMP1 by immunoblotting.
786
787 RNA isolation and cDNA synthesis
788 QIAshredder columns (QIAGEN) were used to homogenize the preparation when
789 needed and whole RNA was isolated using the RNAeasy Mini Kit (QIAGEN) (human
790 and mouse tissue) or PicoPure RNA isolation Kit (ThermoFisher) (CD8+ T cells).
791 150-1000 ng RNA was used to generate cDNA using iScript cDNA Synthesis Kit
792 (Bio-Rad, ref. 1708890). cDNA from sorted cells was amplified with SsoAdvanced
793 PreAmp Supermix (Bio-Rad, ref. 1725160).
794
795 qRT-PCR
796 Gene expression was analyzed using SYBR green gene expression assays
797 (GoTaq® qPCR Master Mix Promega, ref. A6002). The following mouse genes were
798 used (5´->3´, forward;reverse):
799 *Actin* (GGCACCACACCTTCTACAATG; GTGGTGGTGAAGCTGTAGCC),
800 *Timp1* (GAGACACACCAGAGCAGATACC; TGGTCTCGTTGATTTCTGGGG),
801 *Gzmk* (GCCATTTATGGCGTCCATCC; CCGGACTGAAGTCGTGAGAA),
802 *Gzmb* (CAGGAGAAGACCCAGCAAGTCA; CTCACAGCTCTAGTCCTCTTGG),
803 *S100b* (CTGGAGAAGGCCATGGTTGC; CTCCAGGAAGTGAGAGAGCT),
804 *Itgam* (AAGCAGCTGAATGGGAGGAC; TAGATGCGATGGTGTCGAGC).
805 Quantitative PCR reaction was performed on QuantStudio 6 Flex Real-Time PCR
806 System (Applied Biosystems) and analyzed using the software QuantStudio 6 and 7
807 Flex Software.
808
809 Bulk RNA-seq
810 Total RNA samples (500 ng), with RNA Quality score of 9.4 on average (range 9.0-
811 9.8 on a PerkinElmer LabChip analyzer), were converted into sequencing libraries
812 with the "NEBNext Ultra II Directional RNA Library Prep Kit for Illumina" (NEB
813 #E7760). Briefly, polyA+ fraction is purified and randomly fragmented, converted to
814 double stranded cDNA and processed through subsequent enzymatic treatments of
815 end-repair, dA-tailing, and ligation to adapters. Adapter-ligated library is completed
816 by PCR with Illumina PE primers. The resulting purified cDNA libraries were applied
817 to an Illumina flow cell for cluster generation and sequenced on an Illumina NextSeq
818 550 (with v2.5 reagent kits) by following manufacturer's protocols. Raw images

18

819 generated by the sequencer are submitted to analysis, per-cycle basecalling and
820 quality score assignment with Illumina's RTA (Real Time Analysis) integrated primary
821 analysis software. Conversion of BCL (base calls) binary files to FASTQ format is
822 subsequently performed with Local Run Manager GenerateFASTQ Analysis Module
823 (Illumina). Eightysix-base-pair single-end sequenced reads followed adapter and
824 polyA tail removal as indicated by Lexogen. Mouse reads were analysed with the
825 Nextpresso (https://doi.org/10.2174/1574893612666170810153850) pipeline as
826 follows: sequencing quality was checked with FastQC v0.11.0
827 (https://www.bioinformatics.babraham.ac.uk/projects/fastqc/). Reads were aligned to
828 the mouse genome (GRCm39) with TopHat-2.0.10(48) using Bowtie 1.0.0(49) and
829 Samtools 0.1.19(50), allowing 3 mismatches and 20 multihits. The Gencode vM26
830 gene annotation for GRCm39 was used. Read counts were obtained with
831 HTSeq(51). Differential expression and normalization were performed with
832 DESeq2(52), filtering out those genes where the normalized count value was lower
833 than 2 in more than 50% of the samples. From the remaining genes, those that had
834 an adjusted p-value below 0.05 FDR were selected.
835
836 <u>Immunofluorescence and immunohistochemistry</u>
837 For immunofluorescence, fixation with PFA 4% at 4° C was applied to tissue prior to
838 slicing of the brain by using a vibratome (250 μm slices) (Leica) or sliding microtome
839 (80 μm slices) (Fisher). Both types of brain slices were blocked in NGS 10%, BSA
840 2%, Triton 0.25% in PBS for 2 hours at room temperature (RT). Primary antibodies:
841 Anti-KI67 (1:500, Abcam, ref. ab15580, 1.500), Anti-HMB45 (1:500, Abcam, ref.
842 ab732), Anti-CD63 (1:100, Santa Cruz, ref. sc-5275), Anti-GFAP (1:1000, Millipore,
843 ref. MAB360), Anti-GFP (1:1000, Aves Labs, ref. GFP-1020), Anti-cleaved-caspase-3
844 (1:500, Cell Signaling, ref. 9661), Anti-CD8 (1:100, Novus Biologicals, ref. NB200-
845 578), Osteopontin (1:100, Santa Cruz, ref. 21742) and Anti-MHC Class 1 H2 Db/H2-
846 D1 (1:100, Abcam, ref. ab25244) were incubated overnight at 4 ºC in blocking
847 solution and the following day for 30 min at RT. After washing in PBS-Triton 0.25%,
848 secondary antibodies: Alexa-Fluor Anti-chicken488, Anti-chicken647, Anti-rabbit555,
849 Anti-mouse555, Anti-mouse488, Anti-mouse647, Anti-rat555 and Anti-rat488
850 (Invitrogen, dilution 1:300) were added in blocking solution and incubated for 2
851 hours. After washing in PBS-Triton 0.25%, nuclei were stained with bisbenzimide (1
852 mg/ml; Sigma) for 7 min at RT.
853 Immunohistochemistry of paraffin embedded tissues was performed at the CNIO
854 Histopathology Core Facility. For the different staining methods, the slides were
855 deparaffinized in xylene and rehydrated by a graded ethanol series to water. Several
856 immunohistochemical reactions were performed on an automated immunostaining
857 platform (AutostainerLink 48, Agilent; Discovery XT-ULTRA, Ventana-Roche).
858 First, antigen retrieval was performed with the appropriate pH buffer and
859 endogenous peroxidase was blocked (3% hydrogen peroxide). The slides were then
860 incubated with the appropriate primary antibody, as detailed in Supplementary Table
861 23, for single, double or triple staining. Following the primary antibody, the slides
862 were incubated with appropriate secondary antibodies and with horseradish
863 peroxidase conjugated visualization systems when needed.
864 The immunohistochemical reaction was revealed using ChromoMap DAB, Discovery
865 Purple or Teal Kit (Ventana, Roche). Nuclei were counterstained with hematoxylin.
866 Finally, slides were dehydrated, rinsed and mounted for microscopic evaluation.
867 Positive controls for primary antibodies were included in each staining series.

868 Lysozyme immunohistochemistry and RNAScope staining method were perform in
869 an automated immunostaining platform (Ventana Discovery ULTRA, Roche),
870 including deparaffination and re-hydrated as a part of the platform protocol with the
871 appropriate probe: Tissue inhibitor of metalloproteinase 1(TIMP1) mRNA (ACD, ref.
872 567849 for human and ACD, ref. 316849 for mouse). After the probe, slides were
873 incubated with the corresponding Probe Amplification kit (RNAScope VS Universal
874 HRP Detection Reagent, ACD, ref. 323210), conjugated with horseradish peroxidase
875 and reaction was developed using 3, -diaminobenzidine tetrahydrochloride (DAB
876 Detection Kit, Ventana, Roche, ref. 760-224).
877

878 Proximity ligation assay
879 Interaction between CD63 and TIMP1 was investigated using *In situ* Duolink
880 (Duolink® In Situ Orange Starter Kit Mouse/Rabbit, ref. DUO92102) according to
881 manufacturer´s instructions. Paraffin sections were deparaffinized, and antigen
882 retrieval was done by HIER in citrate buffer high pH. Next, sections were blocked for
883 one hour at 37 ºC and incubated with Anti-TIMP1 antibody (1:1000, Dako, ref.
884 M6793) and Anti-CD63 antibody (1:500, Sigma, ref. HPA010088) for 30 min at 37 ºC.
885 Proximity ligation assay probes were added, and the sections were incubated for one
886 hour at 37 °C followed by ligase oligonucleotides added for 30 min at 37 °C. Finally,
887 amplification solution was added for 100 min at 37 °C. Then, slides were incubated
888 with Anti-GFAP (1:500, Abcam, ref. ab4674) and Anti-CD8 (1:100, Novus Biologicals,
889 ref. NB200-578) antibodies for one hour at room temperature (RT) followed by
890 several washes and incubation for one hour at RT with secondary antibodies
891 (Invitrogen, dilution 1:300). Coverslips were mounted using DAPI to visualize cell
892 nuclei. Only primary antibodies or omission of primary antibodies were used as
893 negative controls.
894

895 Image acquisition and analysis
896 Sample selection for analysis was done based on expert histopathological
897 evaluation.
898 Images were acquired with a Leica SP5 up-right confocal microscope 10X, 20X, 40X
899 and 63X objectives and analyzed with ImageJ software. Whole slides were acquired
900 with a slide scanner (AxioScan Z1, Zeiss) and images were captured with Zen Blue
901 software (V3.1 Zeiss). Human samples were analyzed with QuPath[53].
902

903 Multiplex immunohistochemistry
904 To investigate the immune architecture of human and murine brain metastases, we
905 employed Opal technology (Akoya Biosciences, Menlo Park, CA, USA) which allows
906 simultaneous imaging of several markers within one tissue section. The staining was
907 performed on a Ventana Discovery Ultra instrument (Ventana Medical Systems,
908 Basel, Switzerland) and imaged using the Vectra 3 automated quantitative pathology
909 imaging system (Akoya Biosciences) as described previously[54]. In brief, FFPE
910 samples were deparaffinised, rehydrated, and subjected to heat-mediated antigen
911 retrieval for 32 min at 95 °C in cell conditioning solution (CC)1 (Ventana Medical
912 Systems, pH9). Upon incubation of the primary antibody according to Supplementary
913 Table 24, the matching horseradish peroxidase (HRP)-coupled secondary OmniMap
914 antibody (Ventana Medical Systems) was added for 12 min at 36 °C. Following, the
915 signal was detected by incubation of the matching Opal fluorophore (Akoya
916 Biosciences) for 8 min at RT. Afterwards, the antibody complex was removed by
917 heat-mediated stripping with CC2 buffer (Ventana Medical Systems, pH6) for 24 min

20

918 at 100 °C. The incubation of primary antibody, secondary antibody, fluorophore and
919 subsequent heat treatment was repeated until all markers were detected. Finally,
920 nuclei were counterstained with DAPI (Merck, Darmstadt, Germany) and slides were
921 mounted with a coverslip using fluoromount G medium (SouthernBiotech,
922 Birmingham, Alabama, USA). After whole-scanning (x100) of sections using the
923 Vectra 3.0 Automated Imaging System (Akoya Biosciences), regions of interest were
924 defined in Phenochart™ software (Akoya Biosciences) and multispectral images
925 (MSIs) were acquired (x200 magnification). The imaging data was then quantified
926 using inForm (Akoya Biosciences) and R software. Briefly, MSIs were unmixed using
927 a previously built library consisting of single stained tissue slides for all used
928 fluorophores and DAPI. Subsequently, tissue segmentation and cell segmentation
929 were performed. For quantification of stained cells, a self-learning approach was
930 applied to phenotype all cell types. The downstream analyses were performed in R
931 software using the add-ins phenoptr and phenoptrReports (Akoya Biosciences).
932
933 Single-cell RNA sequencing
934 Mouse brains were extracted in pre-cooled D-PBS 1X and were processed with the
935 Adult Brain Dissociation Kit (Miltenyi, ref. 130-107-677) using gentleMACS C Tubes
936 (Miltenyi, ref. 130-093-237) and the gentleMACS™ Octo Dissociator (Miltenyi, ref.
937 130-096-427). Cell suspension was filtered with a 70 μm strainer and was
938 centrifuged at 300 g for 10 min at 4 °C. For myelin removal, the protocol described
939 by Korin et al(55) was followed. Pellet was resuspended with 7 ml of RPMI-1640, at
940 room temperature and 3 ml of SIP solution (Stock isotonic Percoll, ref. GE17-0891-
941 02 Sigma Aldrich) was added to each tube mixing gently. Gradually the 30% (vol/vol)
942 percoll/cell mixture was layered on top of 2ml of 70% (vol/vol) SIP in PBS 1X.
943 Samples were centrifuged at 500g, 30 min, 18 °C, with minimal deceleration. The top
944 layer of myelin was removed using a 10 ml pipette and the solution containing all
945 cellular fractions was centrifuged at 500g, 7 min, 18 °C. The supernatant was
946 discarded and the cells ready for staining were diluted in cold D-PBS/BSA buffer
947 0.5%. Cell suspension was magnetic labelled with Anti-ACSA-2 (Miltenyi, ref. 130-
948 097-678) microbeads and the enrichment in glial populations was checked by flow
949 cytometry (BD FACSCanto II) with Anti-ACSA-2-PE (1:100, Miltenyi, ref. 130-123-
950 284). For dead cell removal and washing prior to single cell sequencing, Debris
951 Removal solution (Miltenyi, ref. 130-109-398) was used. The effluent containing the
952 live cell fraction was centrifuged at 300g for 10 min, washed and finally resuspended
953 in 1X PBS containing 0.04% BSA in a concentration of 7 x 105 cells/ml, placing the
954 cells on ice. Cells suspended in PBS-BSA were tested for the optimal viability and
955 free of debris and aggregates. Cell sample was loaded onto a 10x Chromium Single
956 Cell controller chip B (10x Genomics) as described in the manufacturer's protocol
957 (Chromium Single Cell 3'GEM, Library & Gel Bead Kit v3, ref. PN-1000075).
958 Intended targeted cell recovery of ~10000 cells. Generation of gel beads in emulsion
959 (GEMs), barcoding, GEM-RT clean-up, cDNA amplification and library construction
960 were all performed as recommended by the manufacturer. scRNA-seq libraries were
961 sequenced with an Illumina NextSeq 550 (using v2.5 reagent kits) in paired-end
962 fashion (28bp + 56bp bases). The bollito(56) pipeline was used to perform read
963 analysis, as follows: Sequencing quality was checked with FastQC
964 (http://www.bioinformatics.babraham.ac.uk/projects/fastqc/). Reads were aligned to
965 the mouse reference genome (GRCm38, vM25 gene annotation from
966 GENCODE(57) with STARsolo (STAR 2.7.3a) (58). Seurat 3.2.2(59) was used to
967 check the quality of sequenced cells, explore and quantify single-cell data, obtain cell

968 clusters and specific gene markers. For the annotation of the different cell subtypes,
969 signatures from Zeisel et al. 2015(60); Habib et al. 2020(61) and Batiuk, Martirosyan
970 et al. 2020(62) were used. For astrocytes annotation, signatures in SuppTable13
971 were applied.
972 For analyzing potential interaction among clusters, we calculated the differential
973 expressed genes for each cluster and ran a protein-protein interaction (PPI) network
974 analysis with STRING database(63) information. Ligand-receptor interactions
975 between cluster 3 and cluster 7 were selected and filtered based on experimental
976 and combined scores.
977 In the case of human samples, for which written informed consent was obtained from
978 all patients included in this study, Chromium Fixed RNA Profiling was used (10X
979 Genomics). 25-50 mg of fresh biopsies were fixed in 1 ml of Fixation Buffer
980 containing 4% Formaldehyde. After 22 hours at 4 ºC, fixed tissue was digested with
981 a liberase-based solution using gentleMACS™ Octo Dissociator (Miltenyi, ref. 130-
982 096-427) and the following protocol: 20 min at 37°C, 50 rpm, spin for 30 sec at 37°C,
983 2,000 rpm (clockwise) and spin for 30 sec at 37°C, 2,000 rpm (counter clockwise).
984 Then, sample was kindly centrifuge and pellet was resuspended in 1ml of chilled
985 Quenching buffer. After cell counting and for long term storage, glycerol (10 %) and
986 Enhancer were added for cryopreservation. Fixed cell suspensions obtained with the
987 Chromium Next GEM Single Cell Fixed RNA Sample Preparation Kit (10xGenomics
988 PN-1000414) were processed with the Chromium Fixed RNA Profiling Reagent Kit
989 according to the manufacturer's instructions (10xGenomics, user guide CG000527).
990 Briefly, samples were hybridised to a human transcriptome probe set (Chromium
991 Fixed RNA Kit, 10xGenomics PN1000474) and encapsulated in gel beads in
992 emulsion (GEMs) in a Chromium iX instrument (10xGenomics). GEM recovery and
993 gene expression library construction were all performed as recommended by the
994 manufacturer. Libraries were sequenced with an Illumina NextSeq 550 (using v2.5
995 reagent kits) in paired-end fashion (28bp + 56bp bases). Raw images generated by
996 the sequencer are submitted to analysis, per-cycle basecalling and quality score
997 assignment with Illumina's Real Time Analysis integrated primary analysis software
998 (RTA v2). Conversion of BCL (base calls) binary files to FASTQ format is
999 subsequently performed with bcl2fastq2 (Illumina). For data analysis, cellranger-
1000 7.0.0 was used to generate the count matrices that then were subjected to QC
1001 procedures in R to discard cells with low counts across all genes. Filtered matrices
1002 were normalized by scaling normalization(64) using the Batchelor R package
1003 (https://bioconductor.org/packages/release/bioc/html/batchelor.html). Dimensionality
1004 reduction, graph-based cell clustering and cluster visualization using the Scran R
1005 package (https://bioconductor.org/packages/release/bioc/html/scran.html) were
1006 performed. Clusters were automatically annotated as described in Wang et al. (65).
1007 SingleR was used to predict the cell type using the Human Primary Cell Atlas(66) as
1008 reference. Doublet detection on clustering results was based on two approaches
1009 from the scDblFinder R package
1010 (https://bioconductor.org/packages/release/bioc/html/scDblFinder.html). The first
1011 approach detects doublets as clusters with expression profiles lying between two
1012 other clusters, and the second involves artificially stimulating doublets from the
1013 expression data and then training a classifier to identify putative doublet calls among
1014 real cells. For integration, datasets were corrected for differences in gene detection
1015 and sequencing depth. Batch effects were addressed using the Mutual Nearest
1016 Neighbors (MNN) with the fastMNN function of the batchelor package(67).
1017

1018 <u>Flow cytometry</u>
1019 Cell suspensions were obtained from brains processed according to Korin et al. (55)
1020 or from the spleen of 10–15-week-old C57BL/6 mice. For T cells *in vitro* experiments,
1021 spleens were pressed through a 70 μm cell strainer and red blood cells were lysed
1022 with ACK Lysing Buffer (Lonza, ref. 10-548E). For intracellular stainings of CD8+ T
1023 cells *in vitro* culture, eBioscience Cell Stimulation Cocktail (plus protein transport
1024 inhibitors) (500X) were used (2 μl per ml, Invitrogen, ref. 00-4975-9). Resulting cells
1025 suspensions were incubated for 10 min with Fc Block (1:100, BD Biosciences, ref.
1026 553141) in staining buffer (ebioscience, ref. 00-4222-26) and incubated for 30 min
1027 with the corresponding primary antibodies (SuppTable 25) in staining buffer. In the
1028 case of intracellular stainings, D Cytofix/Cytoperm™ Fixation/Permeabilization Kit
1029 (BD Biosciences, ref. 554714) was used. After washing, cells were resuspended in
1030 staining buffer and acquired either on a FACS Symphony, LSR Fortessa X20 or
1031 FACSCanto II flow cytometers (BD Biosciences) with optimised settings through
1032 voltration experiments. Cell sorting experiments were carried out on a FACSAria IIu
1033 cell sorter (BD Biosciences).
1034
1035 <u>Rhapsody</u>
1036 For tissue dissociation, mouse brains were transferred to RPMI-1640 medium and
1037 dissociated gently using a 15-ml dounce homogenizer and then, the protocol
1038 described by Korin et al(55) was followed. Top layer of myelin was removed, cells
1039 from the interphase were collected with a Pasteur pipette and washed with Staining
1040 Buffer (PBS-/-, containing 5% FBS and 2 mM EDTA). Cells were centrifuged (10.000
1041 G, 1 min, 4 ºC) and stained for flow cytometry. Target population (DAPI-
1042 CD45+CX3CR1-) was sorted in a FACSAria Fusion sorter (BD Biosciences) into
1043 1.5 mL Lowbind Eppendorf tubes (Eppendorf, ref. 0030122348). In some cases, cells
1044 were separated by magnetic beads using Mouse CX3CR1 positive Selection Kit
1045 (MojoSort, ref. 480056) to remove unwanted cells, and the negative fraction was
1046 collected in Lowbind Eppendorf tubes. For scRNA-seq cell capture, library
1047 preparation, sequencing and analysis, each sample was barcoded with the Single
1048 Cell Labelling of BD™ Single-Cell Multiplexing kit following manufacturer's
1049 instructions. Single cell capture and cDNA synthesis preparation were performed
1050 following manufacturer's instructions with the BD Rhapsody™. mRNA Targeted and
1051 Sample Tag Library Preparation were prepared according to BD Rhapsody™
1052 Targeted mRNA and AbSeq Amplification Kit protocol using BD Rhapsody™ Immune
1053 Response Panel Mm kit (ref. 633753). The concentration of PCR products and
1054 amplified libraries were determined with a Qubit fluorometer using the Qubit®dsDNA
1055 HS assay kit (Invitrogen, ref. Q32854). Their size distribution was assessed running
1056 an aliquot on an Agilent Technologies 2100 Bioanalyzer, using an Agilent High
1057 Sensitivity DNA Chip (Agilent Technologies, ref. 5067-4626). Sequencing was
1058 performed in a NovaSeq 6000 system. Library demultiplexing and targeted gene-
1059 expression library were aligned using Seven Bridges Genomics platform following
1060 the BD Biosciences Rhapsody pipeline (BD Biosciences). Cell clustering and gene
1061 expression analysis was performed using Seurat v4.1.1(68).
1062
1063 <u>T cells *in vitro* culture</u>
1064 CD8+ T cells were obtained from the spleen of 10-15 weeks old C57BL/6 female
1065 mice. The whole organ was pressed through a 70-μm cell strainer and red blood
1066 cells were lysed with ACK Lysing Buffer (Lonza, ref. 10-548E). Cells were
1067 resuspended in HBSS 1X supplemented with 2% FBS and 1 mM EDTA at a

1068   concentration of 108 cells/ml. EasySep™ Mouse Total CD8+ T Cell Isolation Kit
1069   (STEMCELL, ref. 19853A) protocol was followed as indicated by the manufacturer to
1070   select total CD8+ T cells. Dynabeads™ Mouse T-Activator CD3/CD28 (Thermo
1071   Scientific, ref. 11456D) were used to activate the CD8 T cells in culture. After 24
1072   hours, the dynabeads were removed from the culture with the help of a magnetic
1073   particle concentrator. CD8+ T cells were cultured in RPMI-1640 medium
1074   supplemented with 10% FBS, 2 mM L-glutamine, 1 mM Sodium Pyruvate, 100 IU/ml
1075   penicillin/streptomycin, 50 µM ß-Mercaptoethanol,1 mM Hepes and Human IL2
1076   (Miltenyi, ref. 130097743). When using CD8+T cells sorted from the spleen, T cells
1077   were activated with anti-mouse CD3e clone 145-2C11 (1 µg/ml, BD Biosciences, ref.
1078   553066) coated plates, soluble anti-mouse CD28 (37.51) (1 µg/ml, Tonbo
1079   Biosciences, ref. 70-0281-U500) and mouse IL-2 (0.1 µg/ml, Miltenyi Biotec, ref.
1080   130-094-054), in RPMI medium supplemented with 10% FBS and Penicillin-
1081   Streptomycin. CD8+ T cells were maintained in culture for one day before
1082   conditioned medium (CM) from STAT3+ and STAT3- astrospheres was added. Two
1083   to three days after addition of CM, flow cytometry was performed using the
1084   appropriated conjugated antibodies. Activated CD8+ T cells incubated with CM from
1085   astrospheres were added to B16/F10-BrM cells in a ratio 1:5 (cancer cell: CD8+ T
1086   cell) for viability assays that were analyzed by bioluminescence.
1087   OT-I T cells extracted from the spleen of Tg(TcraTcrb)1100Mjb/J and maintained in *in*
1088   *vitro* culture after stimulation with 40 pM OVAlbumin-derived SIINFEKL peptide(29)
1089   were used in cytolysis assays in a ratio 1:4 (cancer cell: CD8+ T cell).
1090   Anti-TIMP1 antibody (102D1) (10 µg/ml, Thermofisher, ref. MS608PABX) or rTIMP1
1091   (100 ng/mL, R&D Systems, ref. 980-MT) were added at day 0 when indicated.
1092
1093   <u>Phosphoproteomics</u>
1094   CD8+ T cells were obtained from the spleen of 10-15 weeks old C57BL/6 female
1095   mice and selected, activated and expanded as described above by using EasySep™
1096   Mouse Total CD8+ T Cell Isolation Kit (STEMCELL, ref. 19853A). After conditioned
1097   medium (CM) from astrospheres was added, cell density was maintained at 500,000
1098   cells/ml. Two days after addition of CM, T cells pellet was washed with PBS 1X three
1099   times and sample was prepared for proteomic analysis.
1100   Lymphocytes were lysed 15 minutes at 95 °C in 5% SDS, 100mM Tris/HCl pH 8.0.
1101   After cooling, lysate was incubated at 25 ºC with 10 units of DNAse (Benzonase,
1102   Merk) and sonicated 10 minutes in a Bioruptor for DNA shearing. Protein
1103   concentration was determined using BSA as standard. Then, samples were digested
1104   using on bead protein aggregation capture (PAC) with MagReSyn® Hydoxyl
1105   microparticles (ratio Protein/Beads 1:5) in an automated King Fisher instrument
1106   (Thermo). Proteins were digested 16 h at 37 ºC, with 300 µl of a mixture of
1107   trypsin/LysC in 50 mM TEAB pH 8.0 (Trypzean trypsin, Sigma, LysC endoprotease,
1108   Wako, protein:enzyme ratio 1:100 each). Resulting peptides were speed-vac dried
1109   and re-dissolved in 100 µl of 200 mM HEPES pH 8.5.
1110   Samples (approximately 100 µg) were labeled 1 h at 25 ºC using Thermo Scientific
1111   TMTpro 18plex™ Isobaric Label Reagent. Reaction was quenched/stopped by
1112   adding 5% hydroxylamine. Samples were mixed in 1:1 ratio based on total peptide
1113   amount, which was determined from an aliquot by comparing overall signal
1114   intensities on a regular LC-MS/MS run. The final mixture was finally desalted using a
1115   Sep-Pak C18 cartridge (Waters) and dried prior high pH reverse phase HPLC pre-
1116   fractionation.

24

1117 Labeled peptides were pre-fractionated offline by means of high pH reverse phase
1118 chromatography using an Ultimate 3000 HPLC system equipped with a sample
1119 collector. Briefly, peptides were dissolved in 100 µL of phase A (10 mM NH4OH) and
1120 loaded onto a XBridge BEH130 C18 column (3.5 µm, 150 mm length and 1 mm ID)
1121 (Waters). Phase B was 10 mM NH4OH in 90% CH3CN. The following gradient (flow
1122 rate of 100 µL/min) was used: 0-50 min 0-25% B, 50-56 min 25-60% B, 56-57 min
1123 60-90% B. One-minute fractions from minute 15 to 65 were collected, neutralized
1124 with 10 µl of 10% formic acid and immediately vacuum dried. Based on the UV
1125 absorbance at 280nm, 40 fractions were pooled in 8 fractions for phosphopeptide
1126 enrichment.
1127 Phosphopeptides were enriched with MagReSyn® Zr-IMAC HP beads in an
1128 automated King Fisher instrument, using the manufacturer protocol. Eluted fractions,
1129 enriched in phosphopeptides, were immediately acidified with 10% formic acid and
1130 dry in a vacuum dryer. Flowthrough for each pool was further fractionated by micro
1131 RP-High PH in four fractions and kept for total proteome analysis.
1132 LC-MS/MS was done by coupling an UltiMate 3000 RSLCnano LC system to an
1133 Orbitrap Exploris 480 mass spectrometer (Thermo Fisher Scientific). Samples were
1134 loaded into a trap column (Acclaim™ PepMap™ 100 C18 LC Columns 5 µm, 20 mm
1135 length) for 3 min at a flow rate of 10 µl/min in 0.1% FA. Then, peptides were
1136 transferred to an EASY-Spray PepMap RSLC C18 column (Thermo) (2 µm, 75 µm x
1137 50 cm) operated at 45 °C and separated using a 90 min effective gradient (buffer A:
1138 0.1% FA; buffer B: 100% ACN, 0.1% FA) at a flow rate of 250 nl/min. The gradient
1139 used was, from 4% to 6% of buffer B in 5 min, from 6% to 25% B in 70 minutes, from
1140 25% to 45% B in 14 minutes, plus 10 additional minutes at 98% B.
1141 The mass spectrometer was operated in a data-dependent mode, with an automatic
1142 switch between MS and MS/MS scans using a top 15 method. (Intensity threshold ≥
1143 5e4, dynamic exclusion of 20 sec and excluding charges unassigned, +1 and ≥ +6).
1144 MS spectra were acquired from 350 to 1500 m/z with a resolution of 60,000 FMHW
1145 (200 m/z). Ion peptides were isolated using a 0.7 Th window and fragmented using
1146 higher-energy collisional dissociation (HCD) with a normalized collision energy NCE
1147 of 36. MS/MS spectra were acquired with a fixed first mass of 120 m/z and a
1148 resolution of 45,000 FMHW (200 m/z). The ion target values were 3e6 for MS
1149 (maximum IT 25 ms) and 1e5 for MS/MS (maximum IT, auto). For data analysis, raw
1150 files were processed with MaxQuant (v 2.1.4.0) using the standard settings against a
1151 mouse protein database (UniProtKB/TrEMBL, 21,990 sequences) supplemented
1152 with contaminants. Carbamidomethylation of cysteines was set as a fixed
1153 modification whereas oxidation of methionines, protein N-term acetylation,
1154 phosphorylation of S, T, Y and N/Q de-amidation as variable modifications. Minimal
1155 peptide length was set to seven amino acids and a maximum of two tryptic missed-
1156 cleavages were allowed. Results were filtered at 0.01 FDR (peptide and protein
1157 level).
1158 Afterwards, the phosphosite or protein intensities files were loaded in Prostar
1159 (v1.30.0) (Wieczorek et al, Bioinformatics 2017) (69) using the intensity values for
1160 further statistical analysis. Briefly, proteins/sites with less than eighteen valid values
1161 were filtered out. Then, a global normalization of log2-transformed intensities across
1162 samples was performed using the LOESS function. Differential analysis was done
1163 using the empirical Bayes statistics Limma. Proteins with a p.value < 0.05 and a log2
1164 ratio > 0.3 or < -0.3 were defined as regulated. The FDR was estimated to be below
1165 5% by Benjamini-Hochberg.
1166

25

1167 <u>Sampling of human tissues</u>
1168 Human brain metastasis tissue, peripheral blood and cerebrospinal fluid (CSF) were
1169 collected by CNIO Biobank as backbone of a collaborative nationwide multicenter
1170 cohort, RENACER, integrated by 19 different hospitals and coordinated from CNIO
1171 Biobank. Written informed consent from each donor is collected from each patient
1172 included in this study and surplus diagnostic samples are shipped to CNIO in less
1173 than 24h from surgery, under controlled temperature and other pre-analytical
1174 variables, to warranty homogeneity and quality of the cohort. All the studies were
1175 conducted in accordance with recognized ethical guidelines (Declaration of Helsinki)
1176 and were approved by our Institutional Review Board (IRB) (CEI PI 25_2020-3).
1177 Comprehensive clinical information is also collected by CNIO Biobank associated to
1178 the samples.
1179
1180 <u>Patient-derived organotypic brain cultures</u>
1181 Surgically-resected human brain metastases which have the advantage of including
1182 the immune tumor microenvironment from patients with lung cancer (7 cases), breast
1183 cancer (2 cases), melanoma (4 cases) or other primary sources (2 cases), were
1184 obtained from the CNIO Biobank that previously received them from Hospital
1185 Universitario 12 de Octubre, Complejo Hospitalario Universitario de Albacete,
1186 Hospital Álvaro Cunqueiro Vigo, Complejo Universitario de Navarra, Hospital
1187 Universitario de Burgos and Hospital Universitario de Bellvitge. All samples were in
1188 compliance with protocols approved by our Institutional Review Board (IRB) (CEI PI
1189 25_2020-3). Written informed consent was signed by all patients included in this
1190 study. PDOCs were generated as described previously(70). Briefly, after
1191 neurosurgical resection, brain metastasis samples were directly collected in
1192 Neurobasal-A media (ThermoFisher Scientific, ref. 21103049) supplemented with
1193 1 μg/ mlamphotericin B, 100 IU/ml penicillin/streptomycin, 25 ng/ml basic human
1194 fibroblast growth factor, 100 ng/ml IGF1, 25 ng/ ml EGF, 10 ng/ml neuroregulin-1 β1
1195 (NRG1; R&D Systems, ref. 396-HB) 1× N-2 supplement (Gibco, ref. 17502048) and
1196 1× B27 supplement. Organotypic brain cultures were prepared as described above.
1197 Slices from brain metastases were cultured in the presence of human IgG (BioXell,
1198 ref. BE0092), Anti-TIMP1 (Thermofisher, ref. MS608PABX) and Anti-CD8 (BioXcell,
1199 ref. BE0004-2) at 10 μg/μl for three days. Brain slices were fixed in 4% PFA
1200 overnight at 4 °C, and then free-floating immunofluorescence was performed.
1201 Proliferation was evaluated by manually counting Ki67+ nuclei from cancer cells.
1202
1203 <u>Spheroids assays</u>
1204 Human samples were disaggregated mechanically, ACK Lysing Buffer (Lonza, ref.
1205 10-548E) was used to lysis red cells and the samples were digested with DMEM
1206 supplemented with 0.125% collagenase III and 0.1% hyaluronidase at 37 ºC for 45
1207 min. After PBS 1x washing, cells were resuspended in Neurobasal-A media
1208 supplemented as described for PDOCs, and astrospheres conditioned medium (CM)
1209 and drugs were added (Anti-TIMP1, 10μg/ml, Thermofisher, ref. MS608PABX).
1210 Spheroids were maintained in culture in low attachment plates for a maximum of
1211 three days. For immunofluorescence staining, spheroids were fixed using
1212 CytoSpin™ (Thermo Scientific) and paraformaldehyde (4%).
1213
1214 <u>Clinical samples</u>
1215 Brain metastases from lung cancer (7 cases), breast cancer (3 cases), melanoma
1216 (11 cases) or from other primary origins (4 cases) were obtained from the CNIO

1217 Biobank that previously received them from Hospital Universitario 12 de Octubre,
1218 Complejo Hospitalario Universitario de Albacete, Hospital Álvaro Cunqueiro Vigo,
1219 Complejo Universitario de Navarra, Hospital Universitario de Burgos and Hospital
1220 Universitario de Bellvitge. All samples were in compliance with protocols approved
1221 by our Institutional Review Board (IRB) (CEI PI 25_2020-3) and the Institutional
1222 Review Board of Department of Neuroscience, University of Turin. Written informed
1223 consent was signed by each patient include in this study. Cases were selected to
1224 include only samples with peritumoral tissue in order to evaluate the
1225 microenvironment surrounding brain metastasis. Immunohistochemistry was
1226 performed at the CNIO Histopathology Core Facility using standardized automated
1227 protocols and multiplex was performed at Institute of Immunology (Faculty of
1228 Medicine Carl Gustav Carus).
1229
1230 <u>TIMP1 detection in liquid biopsies</u>
1231 To determine the concentration of TIMP1 in mice plasma, around 500 μL of blood
1232 were centrifuged (500 g for 10 min at 10 ºC, and the resulting supernatant fraction,
1233 again at 3,000 g for 20 min at 10 °C) immediately after the extraction. For detection
1234 of TIMP1 secreted in mice cerebrospinal fluid (CSF), CSF was extracted from the
1235 cisterna magna of anesthetized animals with a capillary tube, then it was centrifuged
1236 600g for 5min at 4ºC. TIMP1 levels were measured using ELISA as indicated by the
1237 manufacturer (Sigma Aldrich, ref. RAB0468).
1238 For liquid biopsies a patient cohort of 6 plasma samples from non-cancer patients
1239 were obtained from Center for Applied Clinical Research (CIMA)-Navarra University,
1240 patients with lung cancer brain metastasis (6 cases), breast cancer brain metastasis
1241 (2 cases), melanoma brain metastasis (1 case) and brain metastasis with other
1242 primary tumors (2 cases) were obtained from the CNIO Biobank that previously
1243 received them from Hospital Universitario 12 de Octubre and Hospital Álvaro
1244 Cunqueiro Vigo. CSF samples from 5 non-cancer patients were obtained from the
1245 Biobank of Hospital Universitario Virgen de la Macarena, patients with lung cancer
1246 brain metastasis (6 cases), breast cancer brain metastasis (2 cases), melanoma
1247 brain metastasis (1 case) and brain metastasis with other primary tumors (2 cases)
1248 were obtained from the CNIO Biobank that previously received them from Hospital
1249 Universitario 12 de Octubre and Hospital Álvaro Cunqueiro Vigo. All samples were in
1250 compliance with protocols approved by their respective institutional review board
1251 (IRB) (B.0001601, CEI PI 25_2020-v2 and CEI PI 25_2020-3). Written informed
1252 consent was signed by each patient included in this study. TIMP1 levels in patients'
1253 plasma and CSF were measured by ELISA following the manufacturer's instructions
1254 (Sigma Aldrich, ref. RAB0466).
1255
1256 <u>Survival analysis</u>
1257 Survival data of 10 patients with brain metastases from different solid tumors were
1258 available. Mean (range) TIMP1 levels of the cohort (5-317 μg/ml) was used to
1259 determine high TIMP1 (>167 ng/ml) and low TIMP1 (<167 ng/ml). Kaplan Meier
1260 product limit method was generated for survival estimations. Log-rank test was
1261 performed to analyze survival differences between TIMP-1 levels in liquor (high vs.
1262 low). A two-sided p-value of <0.05 was considered to indicate statistical significance.
1263
1264 <u>Immune cluster analysis</u>
1265 Transcriptomic data was used to cluster a total of 108 brain metastatic samples into
1266 high, medium and low immune following methodology in García-Mulero et al(26).

27

1267 Gene expression of selected genes was compared between the three groups by
1268 non-parametric methods. To select biomarkers of high immune metastases, the best
1269 combination of marker genes was selected from a list of candidate genes by a binary
1270 decision tree with cross validation (k= 10) that identified the optimal classification
1271 model for high/low differentiation. R package caret was used to perform the
1272 selection. High and Low samples (n= 44) were randomly divided into Training (75%,
1273 n= 33) and Test (25%, n= 11) datasets. The Training datasets was used for
1274 classification and the Testing dataset for evaluation of the prediction accuracy.
1275 Prediction accuracy was evaluated by calculating the sensitivity, specificity, and area
1276 under the curve (AUC).
1277 For the validation with samples from the RENACER cohort (n=135) or subcohorts
1278 with specific samples, raw reads preprocessing was performed as detailed:
1279 QuantSeq 3' mRNA-Seq reads from brain metastatic samples were processed
1280 closely following Lexogen's QuantSeq 3' mRNA-Seq Kit and integrated data analysis
1281 pipeline on Bluebee platform (015UG108V0140).FastQC (v.0.11.9) was used to
1282 generate QC reports of the sequencing reads. Raw reads were then trimmed with
1283 bbduk (bbmap v.38.93) to remove both the poly-A tail and adapter sequences.
1284 Trimmed reads were aligned with STAR v2.7.8a(58). to the GRCh38 reference with
1285 custom ENCODE settings as suggested by the aforementioned protocol and indexed
1286 with samtools v1.14(50), Finally, mapped reads were counted and aggregated to
1287 gene level counts with htseq-count v.0.13.5(51) and the Gencode v38
1288 comprehensive gene annotation. For count normalization and batch correction,
1289 normalization and variance-stabilization of the raw counts was performed by
1290 DESeq2 v1.34.0, vst function(52). Then, we used limma v3.50.1(71) to fit a linear
1291 model of the normalized counts including both the batch and the primary site of each
1292 metastatic sample. Afterwards, the batch component was removed using
1293 removeBatchEffect, while preserving the differences associated with the primary site
1294 of the sample. For the immune cluster classification, the normalized and regressed
1295 gene expression matrix was used to assess the immune cluster profile of each
1296 sample and cluster them according to the methods of García-Mulero et al(26). For
1297 the analysis of RENACER cohort or the specified subsets of samples, single sample
1298 enrichment scores were calculated for a set of immune signatures defined by the
1299 authors using the GSVA package(72). Then, samples were grouped by
1300 agglomerative hierarchical clustering with Ward-D2 as linkage method over the
1301 euclidean distance of the enrichment scores. Finally, the resulting dendrogram was
1302 split with the R package dendextend v1.16.0 to generate three categories, each
1303 representing different immune and inflammatory profiles. All the bioinformatic
1304 analyses were carried out in R v4.1.1.
1305
1306 Gene set enrichment analysis
1307 GSEAPreranked(73) was used to perform gene set enrichment analysis for the
1308 selected signature collections on a preranked gene list according to the t-statistic,
1309 setting 1000 gene set permutations. Gene sets with significant enrichment levels
1310 (FDR q-value < 0.25) were considered.
1311
1312 Quantification and statistics
1313 Data was analyzed using GraphPad Prism 8 software (GraphPad Software). For
1314 comparisons between two experimental groups in datasets that followed a normal
1315 distribution, an unpaired, two-tailed Student's t-test was used. For multiple
1316 comparisons, ANOVA test was performed. For survival curves, P values were

obtained with log-rank (Mantel–Cox) two-sided tests. Chi squared test was performed for the comparison of group proportions. For CD8+CD63+ T cells qPCRs a relative scale is used for the representation that takes the minimum and maximum values for each gene.

Datasets and GEO access references
The mass spectrometry proteomics data have been deposited to the ProteomeXchange Consortium via the PRIDE partner repository with the dataset identifier PXD040436. Bulk RNAseq data from CD8+ T cells have been deposited to GEO with the dataset identifier GSE228364. scRNAseq data from experimental brain metastasis have been deposited to GEO with the dataset identifier GSE228368 and scRNAseq data from human samples have been deposited to GEO with the dataset identifier GSE254379. Rhapsody scRNAseq data data have been deposited to GEO with the dataset identifier GSE228379.

Bibliography

1. Valiente M, Ahluwalia MS, Boire A, Brastianos PK, Goldberg SB, Lee EQ, et al. The evolving landscape of brain metastasis. Trends Cancer. 2018;4:176–96.
2. Margolin K, Ernstoff MS, Hamid O, Lawrence D, McDermott D, Puzanov I, et al. Ipilimumab in patients with melanoma and brain metastases: an open-label, phase 2 trial. Lancet Oncol. 2012;13:459–65.
3. Tawbi HA, Forsyth PA, Algazi A, Hamid O, Hodi FS, Moschos SJ, et al. Combined nivolumab and ipilimumab in melanoma metastatic to the brain. N Engl J Med. 2018;379:722–30.
4. Goldberg SB, Schalper KA, Gettinger SN, Mahajan A, Herbst RS, Chiang AC, et al. Pembrolizumab for management of patients with NSCLC and brain metastases: long-term results and biomarker analysis from a non-randomised, open-label, phase 2 trial. Lancet Oncol. 2020;21:655–63.
5. Gadgeel SM, Lukas RV, Goldschmidt J, Conkling P, Park K, Cortinovis D, et al. Atezolizumab in patients with advanced non-small cell lung cancer and history of asymptomatic, treated brain metastases: Exploratory analyses of the phase III OAK study. Lung Cancer. 2019;128:105–12.
6. Long GV, Atkinson V, Lo S, Sandhu S, Guminski AD, Brown MP, et al. Combination nivolumab and ipilimumab or nivolumab alone in melanoma brain metastases: a multicentre randomised phase 2 study. Lancet Oncol. 2018;19:672–81.
7. Tawbi HA, Forsyth PA, Hodi FS, Lao CD, Moschos SJ, Hamid O, et al. Safety and efficacy of the combination of nivolumab plus ipilimumab in patients with melanoma and asymptomatic or symptomatic brain metastases (CheckMate 204). Neuro Oncol. 2021;23:1961–73.
8. Di Giacomo AM, Chiarion-Sileni V, Del Vecchio M, Ferrucci PF, Guida M, Quaglino P, et al. Primary Analysis and 4-Year Follow-Up of the Phase III NIBIT-M2 Trial in Melanoma Patients With Brain Metastases. Clin Cancer Res. 2021;27:4737–45.
9. Eguren-Santamaria I, Sanmamed MF, Goldberg SB, Kluger HM, Idoate MA, Lu BY, et al. PD-1/PD-L1 Blockers in NSCLC Brain Metastases: Challenging Paradigms and Clinical Practice. Clin Cancer Res. 2020;26:4186–97.
10. Pluim D, Ros W, van Bussel MTJ, Brandsma D, Beijnen JH, Schellens JHM. Enzyme linked immunosorbent assay for the quantification of nivolumab and

1367 pembrolizumab in human serum and cerebrospinal fluid. J Pharm Biomed Anal.
1368 2019;164:128–34.

1369 11. Taggart D, Andreou T, Scott KJ, Williams J, Rippaus N, Brownlie RJ, et al. Anti-
1370 PD-1/anti-CTLA-4 efficacy in melanoma brain metastases depends on
1371 extracranial disease and augmentation of CD8+ T cell trafficking. Proc Natl
1372 Acad Sci USA. 2018;115:E1540–9.

1373 12. Maxwell R, Luksik AS, Garzon-Muvdi T, Hung AL, Kim ES, Wu A, et al.
1374 Contrasting impact of corticosteroids on anti-PD-1 immunotherapy efficacy for
1375 tumor histologies located within or outside the central nervous system.
1376 Oncoimmunology. 2018;7:e1500108.

1377 13. Jessurun CAC, Hulsbergen AFC, de Wit AE, Tewarie IA, Snijders TJ, Verhoeff
1378 JJC, et al. The combined use of steroids and immune checkpoint inhibitors in
1379 brain metastasis patients: a systematic review and meta-analysis. Neuro Oncol.
1380 2021;23:1261–72.

1381 14. Tringale KR, Reiner AS, Sehgal RR, Panageas K, Betof Warner AS, Postow
1382 MA, et al. Efficacy of immunotherapy for melanoma brain metastases in
1383 patients with concurrent corticosteroid exposure. CNS Oncol.
1384 2023;12(1):CNS93

1385 15. Valiente M, Obenauf AC, Jin X, Chen Q, Zhang XH-F, Lee DJ, et al. Serpins
1386 promote cancer cell survival and vascular co-option in brain metastasis. Cell.
1387 2014;156:1002–16.

1388 16. Priego N, Zhu L, Monteiro C, Mulders M, Wasilewski D, Bindeman W, et al.
1389 STAT3 labels a subpopulation of reactive astrocytes required for brain
1390 metastasis. Nat Med. 2018;24:1024–35.

1391 17. Gril B, Palmieri D, Qian Y, Anwar T, Liewehr DJ, Steinberg SM, et al.
1392 Pazopanib inhibits the activation of PDGFRβ-expressing astrocytes in the brain
1393 metastatic microenvironment of breast cancer cells. Am J Pathol.
1394 2013;182:2368–79.

1395 18. Xing F, Kobayashi A, Okuda H, Watabe M, Pai SK, Pandey PR, et al. Reactive
1396 astrocytes promote the metastatic growth of breast cancer stem-like cells by
1397 activating Notch signalling in brain. EMBO Mol Med. 2013;5:384–96.

1398 19. Wasilewski D, Priego N, Fustero-Torre C, Valiente M. Reactive astrocytes in
1399 brain metastasis. Front Oncol. 2017;7:298.

1400 20. Álvaro-Espinosa L, de Pablos-Aragoneses A, Valiente M, Priego N. Brain
1401 microenvironment heterogeneity: potential value for brain tumors. Front Oncol.
1402 2021;11:714428.

1403 21. Kantzer CG, Boutin C, Herzig ID, Wittwer C, Reiß S, Tiveron MC, et al. Anti-
1404 ACSA-2 defines a novel monoclonal antibody for prospective isolation of living
1405 neonatal and adult astrocytes. Glia. 2017;65:990–1004.

1406 22. Ma W, Oliveira-Nunes MC, Xu K, Kossenkov A, Reiner BC, Crist RC, et al.
1407 Type I interferon response in astrocytes promotes brain metastasis by
1408 enhancing monocytic myeloid cell recruitment. Nat Commun. 2023;14:2632.

1409 23. Verdura S, Cuyàs E, Llorach-Parés L, Pérez-Sánchez A, Micol V, Nonell-
1410 Canals A, et al. Silibinin is a direct inhibitor of STAT3. Food Chem Toxicol.
1411 2018;116:161–72.

1412 24. Klemm F, Maas RR, Bowman RL, Kornete M, Soukup K, Nassiri S, et al.
1413 Interrogation of the Microenvironmental Landscape in Brain Tumors Reveals
1414 Disease-Specific Alterations of Immune Cells. Cell. 2020;181:1643–1660.e17.

1415 25. Sutter PA, Willis CM, Menoret A, Nicaise AM, Sacino A, Sikkema AH, et al.
1416 Astrocytic TIMP-1 regulates production of Anastellin, an inhibitor of

1417   oligodendrocyte differentiation and FTY720 responses. Proc Natl Acad Sci
1418   USA. 2024;121:e2306816121.
1419   26. García-Mulero S, Alonso MH, Pardo J, Santos C, Sanjuan X, Salazar R, et al.
1420   Lung metastases share common immune features regardless of primary tumor
1421   origin. J Immunother Cancer. 2020;8(1):e000491
1422   27. Valiente M, Ortega-Paino E. Updating cancer research with patient-focused
1423   networks. Trends Cancer. 2024;10:1–4.
1424   28. Oyler-Yaniv A, Oyler-Yaniv J, Whitlock BM, Liu Z, Germain RN, Huse M, et al.
1425   A Tunable Diffusion-Consumption Mechanism of Cytokine Propagation Enables
1426   Plasticity in Cell-to-Cell Communication in the Immune System. Immunity.
1427   2017;46:609–20.
1428   29. Sancho D, Joffre OP, Keller AM, Rogers NC, Martínez D, Hernanz-Falcón P, et
1429   al. Identification of a dendritic cell receptor that couples sensing of necrosis to
1430   immunity. Nature. 2009;458:899–903.
1431   30. Oelmann E, Herbst H, Zühlsdorf M, Albrecht O, Nolte A, Schmitmann C, et al.
1432   Tissue inhibitor of metalloproteinases 1 is an autocrine and paracrine survival
1433   factor, with additional immune-regulatory functions, expressed by
1434   Hodgkin/Reed-Sternberg cells. Blood. 2002;99:258–67.
1435   31. Monteiro C, Miarka L, Perea-García M, Priego N, García-Gómez P, Álvaro-
1436   Espinosa L, et al. Stratification of radiosensitive brain metastases based on an
1437   actionable S100A9/RAGE resistance mechanism. Nat Med. 2022;28:752–65.
1438   32. Grünwald B, Schoeps B, Krüger A. Recognizing the Molecular Multifunctionality
1439   and Interactome of TIMP-1. Trends Cell Biol. 2019;29:6–19.
1440   33. Jung K-K, Liu X-W, Chirco R, Fridman R, Kim H-RC. Identification of CD63 as a
1441   tissue inhibitor of metalloproteinase-1 interacting cell surface protein. EMBO J.
1442   2006;25:3934–42.
1443   34. Warner RB, Najy AJ, Jung YS, Fridman R, Kim S, Kim H-RC. Establishment of
1444   Structure-Function Relationship of Tissue Inhibitor of Metalloproteinase-1 for Its
1445   Interaction with CD63: Implication for Cancer Therapy. Sci Rep. 2020;10:2099.
1446   35. Justo BL, Jasiulionis MG. Characteristics of TIMP1, CD63, and β1-Integrin and
1447   the Functional Impact of Their Interaction in Cancer. Int J Mol Sci.
1448   2021;22(17):9319
1449   36. Pfistershammer K, Majdic O, Stöckl J, Zlabinger G, Kirchberger S, Steinberger
1450   P, et al. CD63 as an activation-linked T cell costimulatory element. J Immunol.
1451   2004;173:6000–8.
1452   37. Schröder J, Lüllmann-Rauch R, Himmerkus N, Pleines I, Nieswandt B, Orinska
1453   Z, et al. Deficiency of the tetraspanin CD63 associated with kidney pathology
1454   but normal lysosomal function. Mol Cell Biol. 2009;29:1083–94.
1455   38. Ansari KI, Bhan A, Liu X, Chen MY, Jandial R. Astrocytic IGFBP2 and CHI3L1
1456   in cerebrospinal fluid drive cortical metastasis of HER2+breast cancer. Clin Exp
1457   Metastasis. 2020;37:401–12.
1458   39. Delgado-Peraza F, Nogueras-Ortiz CJ, Volpert O, Liu D, Goetzl EJ, Mattson
1459   MP, et al. Neuronal and astrocytic extracellular vesicle biomarkers in blood
1460   reflect brain pathology in mouse models of alzheimer's disease. Cells.
1461   2021;10(5):993
1462   40. Pentsova EI, Shah RH, Tang J, Boire A, You D, Briggs S, et al. Evaluating
1463   Cancer of the Central Nervous System Through Next-Generation Sequencing
1464   of Cerebrospinal Fluid. J Clin Oncol. 2016;34:2404–15.
1465   41. De Mattos-Arruda L, Mayor R, Ng CKY, Weigelt B, Martínez-Ricarte F, Torrejon
1466   D, et al. Cerebrospinal fluid-derived circulating tumour DNA better represents

31

1467   the genomic alterations of brain tumours than plasma. Nat Commun.
1468   2015;6:8839.
1469   42.   Miller AM, Shah RH, Pentsova EI, Pourmaleki M, Briggs S, Distefano N, et al.
1470   Tracking tumour evolution in glioma through liquid biopsies of cerebrospinal
1471   fluid. Nature. 2019;565:654–8.
1472   43.   Rubio-Perez C, Planas-Rigol E, Trincado JL, Bonfill-Teixidor E, Arias A,
1473   Marchese D, et al. Immune cell profiling of the cerebrospinal fluid enables the
1474   characterization of the brain metastasis microenvironment. Nat Commun.
1475   2021;12:1503.
1476   44.   El Rassy E, Botticella A, Kattan J, Le Péchoux C, Besse B, Hendriks L. Non-
1477   small cell lung cancer brain metastases and the immune system: From brain
1478   metastases development to treatment. Cancer Treat Rev. 2018;68:69–79.
1479   45.   Giles AJ, Hutchinson M-KND, Sonnemann HM, Jung J, Fecci PE, Ratnam NM,
1480   et al. Dexamethasone-induced immunosuppression: mechanisms and
1481   implications for immunotherapy. J Immunother Cancer. 2018;6:51.
1482   46.   Moore CS, Crocker SJ. An alternate perspective on the roles of TIMPs and
1483   MMPs in pathology. Am J Pathol. 2012;180:12–6.
1484   47.   Niesel K, Schulz M, Anthes J, Alekseeva T, Macas J, Salamero-Boix A, et al.
1485   The immune suppressive microenvironment affects efficacy of radio-
1486   immunotherapy in brain metastasis. EMBO Mol Med. 2021;13:e13412.
1487   48.   Trapnell C, Pachter L, Salzberg SL. TopHat: discovering splice junctions with
1488   RNA-Seq. Bioinformatics. 2009;25:1105–11.
1489   49.   Langmead B, Trapnell C, Pop M, Salzberg SL. Ultrafast and memory-efficient
1490   alignment of short DNA sequences to the human genome. Genome Biol.
1491   2009;10:R25.
1492   50.   Li H, Handsaker B, Wysoker A, Fennell T, Ruan J, Homer N, et al. The
1493   Sequence Alignment/Map format and SAMtools. Bioinformatics. 2009;25:2078–
1494   9.
1495   51.   Anders S, Pyl PT, Huber W. HTSeq — a Python framework to work with high-
1496   throughput sequencing data. Bioinformatics. 2015;31:166–9.
1497   52.   Love MI, Huber W, Anders S. Moderated estimation of fold change and
1498   dispersion for RNA-seq data with DESeq2. Genome Biol. 2014;15:550.
1499   53.   Bankhead P, Loughrey MB, Fernández JA, Dombrowski Y, McArt DG, Dunne
1500   PD, et al. QuPath: Open source software for digital pathology image analysis.
1501   Sci Rep. 2017;7:16878.
1502   54.   Bayerl F, Bejarano DA, Bertacchi G, Doffin A-C, Gobbini E, Hubert M, et al.
1503   Guidelines for visualization and analysis of DC in tissues using multiparameter
1504   fluorescence microscopy imaging methods. Eur J Immunol.
1505   2023;53(11):e2249923
1506   55.   Korin B, Dubovik T, Rolls A. Mass cytometry analysis of immune cells in the
1507   brain. Nat Protoc. 2018;13:377–91.
1508   56.   García-Jimeno L, Fustero-Torre C, Jiménez-Santos MJ, Gómez-López G, Di
1509   Domenico T, Al-Shahrour F. bollito: a flexible pipeline for comprehensive
1510   single-cell RNA-seq analyses. Bioinformatics. 2022;38:1155–6.
1511   57.   Frankish A, Diekhans M, Jungreis I, Lagarde J, Loveland JE, Mudge JM, et al.
1512   GENCODE 2021. Nucleic Acids Res. 2021;49:D916–23.
1513   58.   Dobin A, Davis CA, Schlesinger F, Drenkow J, Zaleski C, Jha S, et al. STAR:
1514   ultrafast universal RNA-seq aligner. Bioinformatics. 2013;29:15–21.
1515   59.   Stuart T, Butler A, Hoffman P, Hafemeister C, Papalexi E, Mauck WM, et al.
1516   Comprehensive Integration of Single-Cell Data. Cell. 2019;177:1888–1902.e21.

60. Zeisel A, Muñoz-Manchado AB, Codeluppi S, Lönnerberg P, La Manno G, Juréus A, et al. Brain structure. Cell types in the mouse cortex and hippocampus revealed by single-cell RNA-seq. Science. 2015;347:1138–42.

61. Habib N, McCabe C, Medina S, Varshavsky M, Kitsberg D, Dvir-Szternfeld R, et al. Disease-associated astrocytes in Alzheimer's disease and aging. Nat Neurosci. 2020;23:701–6.

62. Batiuk MY, Martirosyan A, Wahis J, de Vin F, Marneffe C, Kusserow C, et al. Identification of region-specific astrocyte subtypes at single cell resolution. Nat Commun. 2020;11:1220.

63. Szklarczyk D, Franceschini A, Wyder S, Forslund K, Heller D, Huerta-Cepas J, et al. STRING v10: protein-protein interaction networks, integrated over the tree of life. Nucleic Acids Res. 2015;43:D447-52.

64. Lun ATL, McCarthy DJ, Marioni JC. A step-by-step workflow for low-level analysis of single-cell RNA-seq data with Bioconductor. [version 2; peer review: 3 approved, 2 approved with reservations]. F1000Res. 2016;5:2122.

65. Wang Z, Wang Y, Chang M, Wang Y, Liu P, Wu J, et al. Single-cell transcriptomic analyses provide insights into the cellular origins and drivers of brain metastasis from lung adenocarcinoma. Neuro Oncol. 2023;25:1262–74.

66. Mabbott NA, Baillie JK, Brown H, Freeman TC, Hume DA. An expression atlas of human primary cells: inference of gene function from coexpression networks. BMC Genomics. 2013;14:632.

67. Haghverdi L, Lun ATL, Morgan MD, Marioni JC. Batch effects in single-cell RNA-sequencing data are corrected by matching mutual nearest neighbors. Nat Biotechnol. 2018;36:421–7.

68. Hao Y, Hao S, Andersen-Nissen E, Mauck WM, Zheng S, Butler A, et al. Integrated analysis of multimodal single-cell data. Cell. 2021;184:3573–3587.e29.

69. Wieczorek S, Combes F, Lazar C, Giai Gianetto Q, Gatto L, Dorffer A, et al. DAPAR & ProStaR: software to perform statistical analyses in quantitative discovery proteomics. Bioinformatics. 2017;33:135–6.

70. Zhu L, Retana D, García-Gómez P, Álvaro-Espinosa L, Priego N, Masmudi-Martín M, et al. A clinically compatible drug-screening platform based on organotypic cultures identifies vulnerabilities to prevent and treat brain metastasis. EMBO Mol Med. 2022;14:e14552.

71. Ritchie ME, Phipson B, Wu D, Hu Y, Law CW, Shi W, et al. limma powers differential expression analyses for RNA-sequencing and microarray studies. Nucleic Acids Res. 2015;43:e47.

72. Hänzelmann S, Castelo R, Guinney J. GSVA: gene set variation analysis for microarray and RNA-seq data. BMC Bioinformatics. 2013;14:7.

73. Subramanian A, Tamayo P, Mootha VK, Mukherjee S, Ebert BL, Gillette MA, et al. Gene set enrichment analysis: a knowledge-based approach for interpreting genome-wide expression profiles. Proc Natl Acad Sci USA. 2005;102:15545–50.

Figure legends

Figure 1. Clusters of brain metastasis-associated reactive astrocytes suggest functional diversity including immune-modulation.
A. Schema of the experimental design. Three different brains from C57BL/6J mice intracranially injected with B16/F10-BrM cells were enzymatically digested and

1567 pooled. ACSA-2 labeling was used to enrich the sample in glial cells, obtaining 7762
1568 cells identified as astrocytes. A pool of three brains without tumor were used as
1569 control for comparisons. **B.** Uniform manifold approximation and projection (UMAP)
1570 plot (0.2 resolution) of the different subpopulations of reactive astrocytes in brain
1571 metastasis. Dotted lines surround *Stat3+* clusters. **C.** *Stat3* expression in the
1572 different clusters of brain metastasis-associated astrocytes. Dot size represents the
1573 dimension of the subpopulation compared to total cells and a colored scale indicates
1574 the level of expression: blue, low expression and red, high expression. **D-E.**
1575 Representation of the top upregulated GSEA pathways in Stat3+ astrocytic clusters
1576 of brain metastasis according to the normalized enrichment score (NES) and a cutoff
1577 of P value < 0.05 and FDR < 0.25. ECM, extracellular matrix. Colored pathways
1578 according to the biological category the gene sets belong to, correspond to more
1579 than half of the total pathways analyzed (total percentage of 100%). Detailed
1580 information of the pathways in SuppTable4. **F.** Schema of the experimental design.
1581 Two human brain metastases from a lung cancer and a breast cancer patients were
1582 fixed, digested and profiled for single-cell RNA-sequencing (scRNA-seq), 2612
1583 astrocytes and 1338 astrocytes were identified, respectively. **G.** Uniform manifold
1584 approximation and projection (UMAP) plot (k= 20) of the different subpopulations of
1585 reactive astrocytes in human brain metastasis. Dotted lines surround clusters with
1586 *STAT3* high expression. **H.** *STAT3* expression in the different clusters of brain
1587 metastasis-associated astrocytes. Dot size represents the dimension of the
1588 subpopulation compared to total cells and a colored scale indicates the level of
1589 expression: blue, low expression and red, high expression. **I**. Normalized enrichment
1590 score (NES) of GSEA pathways comparing cluster 3, 4 and 5 of human brain
1591 metastases-associated astrocytes. KEGG_Cytokine-cytokine receptor interaction,
1592 p.adjust=1,05E-05;   Reactome_Extracellular   matrix   (ECM)   organization,
1593 p.adjust=1,03E-03;   Reactome_Signaling   by   Interleukins,   p.adjust=8,65E-03;
1594 Reactome_Antigen   processing: Ubiquitination   &   Proteasome   degradation,
1595 p.adjust=1,67E-02;   Reactome_Cell   Cycle   Checkpoints,   p.adjust=3,43E-03;
1596 Hallmark_Epithelial_mesenchymal_transition (EMT), p.adjust=5E-09; KEGG_ECM-
1597 receptor interaction, p.adjust=7.08E-05; HALLMARK_Interferon_alpha response,
1598 p.adjust=1.11E-02;   KEGG_Proteasome,   p.adjust=6.53E-04;   HALLMARK_Myc
1599 Targets V1, p.adjust=2.88E-07.
1600
1601 **Figure 2. The pro-tumoral role of STAT3+ reactive astrocytes involves immune-**
1602 **modulation.**
1603 **A.** Schema of the experimental design. Green cells: pSTAT3- astrocytes; red cells:
1604 pSTAT3+ astrocytes. Pre-activated CD8+ lymphocytes incubated with conditioned
1605 medium (CM) generated by pSTAT3- and pSTAT3+ astrospheres (as described in
1606 material and methods section) were processed for bulk RNA-sequencing. **B.** GSEA
1607 of Biological Process (GOBP) of T cell activation downregulated in T cells incubated
1608 with pSTAT3+ astrospheres CM compared to pSTAT3- astrospheres CM. n= 3
1609 independent T cells *in vitro* cultures per condition. **C.** Schema of the experimental
1610 design. C57BL/6J mice were intracranially injected with B16/F10-BrM cells, control
1611 brains and brains from mice treated during six days with the STAT3 inhibitor, silibinin
1612 (Legasil® daily 200 mg/kg daily) were processed to obtain the immune infiltrate
1613 fraction, which was depleted from monocytes. Rhapsody system was used to single
1614 cell sequence a total of 3055 immune cells identifying different CD3+ T cells clusters**.**
1615 **D.** Quantification showing the percentage of cytotoxic-like T cells (clusters 4, 7 and
1616 13) (FigS2C-E) in the brain of control and silibinin treated mice. Values are shown in

box-and-whisker plots, where each dot is a mouse and the line in the box corresponds to the median. The boxes go from the upper to the lower quartiles, and the whiskers go from the minimum to the maximum value (n = 8, control mice; n = 9, mice treated with silibinin). P value was calculated using two-tailed t-test between control and silibinin experimental groups. **E.** Schema of the experimental design. Tmx-treated and untreated cKO^{GFAP}-*Stat3* mice intracranially injected with B16/F10-BrM cells were sacrificed at experimental endpoint, their brains were processed to obtain the immune fraction for flow cytometry analysis or sorted for CD3+CD8+ lymphocytes for RNA isolation and qRT-PCR analysis of gene expression. **F.** Representative flow cytometry analysis of Granzyme b expression in CD3+CD8+T cells from control and cKO^{GFAP}-Stat3 brains intracranially injected with B16/F10-BrM cells. **G.** Quantification of the experiment in F. Error bars, s.e.m. Every dot is a different animal (n= 8). The P value was calculated using the two-tailed t-test. **H.** Schema of the experimental design. Brains from untreated or Tmx-treated cKO^{GFAP}-*Stat3* with IgG2 or anti-CD8 (10 mg/kg, every two days starting at day 3 post-inoculation of cancer cells) two weeks after being inoculated with B16/F10-BrM cells intracardially, were analyzed. **I.** Representative images of *ex vivo* brains in H. Images show the BLI intensity. **J.** Quantification of *ex vivo* bioluminescence (BLI). Values are shown in box-and-whisker plots where every dot represents a different animal. Values were obtained from normalizing the *ex vivo* brain signal to the *in vivo* head signal three days after intracardiac injection when treatment was initiated (n = 39/28/28 mice per experimental condition, 8 independent experiments). The P value was calculated using the two-tailed t-test.

Figure 3. TIMP1 and STAT3 in reactive astrocytes correlate with a high immune cluster classifier in human brain metastases.
A. Representative images showing pSTAT3+ TIMP1+ reactive astrocytes (arrows) in different samples: astrospheres enriched in STAT3, established brain metastasis induced by intracardiac inoculation of B16/F10-BrM cells and human breast cancer brain metastasis. Dotted line surrounds the cancer cells (cc). Scale bar, 20 µm. **B.** Schema of the experimental design. Sequencing data from patients' samples with brain metastases were stratified into low, medium and high immune categories or clusters. Immune clusters were calculated according to an initial algorithm and then complemented with a three gene classifier representing key cell types of the microenvironment. **C-D.** *STAT3* (C) and *TIMP1* (D) expression in human samples from low, medium and high immune clusters. Values are shown in box-and-whisker plots, where each dot is a patient and the line in the box corresponds to the median. The boxes go from the upper to the lower quartiles, and the whiskers go from the minimum to the maximum value (n = 32 samples, low; n= 64 samples, medium; n= 12 samples, high). The P value was calculated using the two-tailed t-test. One way ANOVA is shown to compare the three immune categories. **E.** Schema of the experimental design. A cohort of 12 human samples with extended resection including peritumoral microenvironment was used to validate sequencing data with immunohistochemistry (IHC) profile. In the IHC image STAT3+ reactive astrocytes are shown. RA: reactive astrocytes, cc: cancer cells. Scale bar, 40 µm. **F.** Multiplex representative images of low/ medium/ high immune clusters in the cohort of human samples in E. STAT3 staining and *TIMP1* RNAscope were performed in consecutive sections and allocated on the specific patient categories. n= 4 samples in low immune cluster, n= 4 samples in medium immune cluster, n= 4 samples in high immune cluster. Scale bar, 50 µm, magnification 15 µm. **G.** Graph showing the

correlation between the percentage of immune cells as quantified by multiplex and the percentage of *TIMP1+* events per cell in the microenvironment of 12 brain metastasis samples. Dots are colored according to the immune cluster calculated for the cohort of samples: low (green)/ medium (grey)/ high (red) immune clusters. The P value was calculated using the two-tailed t-test. **H.** A representative image of a patient with melanoma brain metastasis treated with immune checkpoint blockade showing pSTAT3+ reactive astrocytes surrounding the brain metastasis lesion next to CD8+ T cells. The patient showed extracranial response, but failed to respond to ICB intracranially. The dotted line surrounds the cancer cells (cc). Scale bar, 15 µm. **I.** Representative image of multiplex in a sample of a patient in H. Magnification showing CD8+ Granzyme b+ T cells (yellow arrows) and CD8+ Granzyme b- T cells (pink arrows). Scale bar, 20 µm. **J.** Quantification of experiment in I. The graph represents the number of pSTAT3+ reactive astrocytes surrounding a CD8+ T cell with or without Granzyme b positivity in a ratio of 100 µm. A total of 40 CD8+T cells from 5 different patients where GRZ+CD8+ T cells could be identified belonging to the cohort in H were quantified. Error bars, s.e.m. Every dot is a different CD8+ T cell. The P value was calculated using the two-tailed t-test.

Figure 4. TIMP1 mediates brain metastasis in a CD8+ T cell-dependent manner.
A. Schema of the experimental design. pSTAT3- and pSTAT3+ *wt* and pSTAT3+ cKO^{GFAP}-*Timp1* conditioned medium (with or without rTIMP1 100 ng/mL or control IgG/Anti-TIMP1 10 µg/ml) was added to CD8+ T cells and cultured with BrM cells in a 1:4 ratio (BrM-OVA cancer cells: OT-I T cells specific for the OVA-derived SIINFEKL peptide) or a 1:5 ratio (BrM cancer cells: CD8+ T cells previously activated). **B.** Quantification of the bioluminescence (BLI) signal from the experiment shown in A and representative images of B16/F10-BrM-OVA derived BLI at the initial time point and 24 hours after adding CD8+ lymphocytes pre-incubated with CM. Light orange condition refers to co-culture of OT-I T cells with B16/F10-BrM no OVA (control for antigen-specific killing). Values correspond to 24 hours BLI normalized to BLI before adding CD8+ T cells expressed in percentage respect to the mean of control experimental condition (BrM cells). Error bars, s.e.m. n =3 different co-cultures per condition. The P value was calculated using the two-tailed t-test. **C-D.** Schema of the experimental design. Control IgG or Anti-TIMP1 (10 µg/ml) were added to the medium in organotypic cultures of mouse brain with B16/F10-BrM established lesions (C) and Patient-Derived-Organotypic-Cultures (PDOC) that include the brain metastasis-associated microenvironment (D). **E.** Quantification of the BLI signal emitted by B16/F10-BrM cells in each brain slice normalized by the initial value obtained at day 0, before the addition of control IgG, Anti-TIMP1 (10 µg/ml) or Anti-CD8 (100 µg/ml). Values are shown in box-and-whisker plots where every dot represents a different organotypic culture and the line in the box corresponds to the median. Whiskers go from the minimum to the maximum value (n = 42 IgG, 39 Anti-TIMP1 and 27 Anti-TIMP1 plus Anti-CD8 independent organotypic cultures). Quantification is accompanied by representative images of wells containing brain organotypic cultures with established B16/F10-BrM metastases grown *ex vivo* for three days. The image shows the BLI intensity in each condition for each brain slice. P values were calculated using the two-tailed t-test. **F.** Quantification of the number of Ki67+ cancer cells found in IgG2 and Anti-TIMP1-treated PDOCs. Values are shown in box-and-whisker plots where every dot represents a patient and each patient is an independent experiment (n= 11). The pie chart shows all BrM-PDOCs quantified in the graph and classified according to the

36

1717 specific primary tumor. P value was calculated using two-tailed t-test. **G.**
1718 Quantification of the number of Ki67+ cancer cells found in IgG2, Anti-TIMP1 (10
1719 µg/ml) and Anti-TIMP1 (10 µg/ml) plus Anti-CD8 (10 µg/ml) PDOCs. Values are
1720 shown in box-and-whisker plots where every dot represents a patient and each
1721 patient is an independent experiment (n= 7). P value was calculated using two-tailed
1722 t-test. **H.** Schema of the experimental design. cKO^{GFAP}-*Timp1* mice were inoculated
1723 with BrM cells intracardially and after two weeks *ex vivo* brain BLI was analyzed. **I-J.**
1724 Representative images of brains from control and cKO^{GFAP}-*Timp1* mice intracardially
1725 injected with B16/F10-BrM (I) or E0771-BrM (J) cells. The image shows the BLI
1726 intensity in each condition. **K-L.** Quantification of *ex vivo* brain BLI. Values are shown
1727 in box-and-whisker plots where every dot represents a different animal. Values were
1728 obtained from normalizing the *ex vivo* brain signal to the *in vivo* head signal
1729 three days after intracardiac injection with either B16/F10-BrM (K) or E0771-BrM (L)
1730 cells (n = 26/29 mice 4 independent experiments in K and n = 28/25 mice 3
1731 independent experiments in L). The P value was calculated using the two-tailed t-
1732 test. **M.** Representative images of CD8+ T cells in metastatic lesions growing in
1733 brains from control or cKO^{GFAP}-*Timp1* mice intracardially injected with E0771-BrM at
1734 experimental endpoint. White arrows indicate CD8+ T cells and red arrow indicate
1735 Ki67+CD8+ T cells. Scale bar, 25 µm, magnification 5 µm. **N.** Quantification of the
1736 total number of CD8+ T cells in control and cKO^{GFAP}-*Timp1* mice intracardially
1737 injected with E0771-BrM at human endpoint. Values are shown in box-and-whisker
1738 plots where every dot represents a different animal. Ten brains were analyzed in
1739 each condition. The P value was calculated using the two-tailed t-test.
1740
1741 **Figure 5. Characterization of the influence of TIMP1 in CD8+ T cells.**
1742 **A.** Schema of the experimental design. pSTAT3- and pSTAT3+ *wt* and pSTAT3+
1743 cKO^{GFAP}-*Timp1* conditioned medium (CM) was added to CD8+ T cells and flow
1744 cytometry analysis was performed. **B.** Representative flow cytometry analysis using
1745 pre-activated CD8+ T cells incubated with conditioned medium (CM) generated by
1746 pSTAT3- and pSTAT3+ *wt* or pSTAT3+ cKO^{GFAP}-*Timp1* astrospheres. **C.**
1747 Quantification of CD25 geometric mean fluorescence intensity (gMFI) in effector
1748 CD8+ T cells from A. Error bars, s.e.m. n =3 different T cells cultures per condition.
1749 The P value was calculated using the two-tailed t-test. **D-E.** Flow cytometry analysis
1750 showing the % of IFN-γ+TNFα+ (D) and exhausted PD1+LAG3+TIM3+CD39+ (E)
1751 CD8+ T cells incubated with conditioned medium (CM) generated by pSTAT3- and
1752 pSTAT3+ *wt* or pSTAT3+ cKO^{GFAP}-*Timp1* astrospheres. Error bars, s.e.m. n =3
1753 different T cells cultures per condition. The P value was calculated using the two-
1754 tailed t-test. **F.** Schema of the experimental design. CD8+ lymphocytes from *wt* and
1755 cKO^{GFAP}-*Timp1* brains intracranially injected with B16/F10-BrM cells were analyzed
1756 by flow cytometry. **G**, **H.** Representative flow cytometry analysis of CD44 (G) and
1757 quantification of the experiment (H). Error bars, s.e.m. Every dot is a different animal
1758 (n= 5 *wt* brains and n= 5 cKO^{GFAP}-*Timp1* brains). The P value was calculated using
1759 the two-tailed t-test. **I**, **J.** Representative flow cytometry analysis of TNFα (I) and
1760 quantification of the experiment (J). Error bars, s.e.m. Every dot is a different animal
1761 (n= 8 wt brains and n= 9 cKO^{GFAP}-*Timp1* brains). The P value was calculated using
1762 the two-tailed t-test. **K**, **L**. Representative flow cytometry analysis of CD39 and PD1
1763 (K) and quantification of the experiment (L). Error bars, s.e.m. Every dot is a different
1764 animal (n= 8 wt brains and n= 9 cKO^{GFAP}-*Timp1* brains). The P value was calculated
1765 using the two-tailed t-test.
1766

1767 **Figure 6. TIMP1 modulates CD8+ T cells through CD63.**
1768 **A.** Schema of the experimental design. CD63 expression was analyzed by flow
1769 cytometry gating on CD8+ T cells from metastasis free and brains intracranially
1770 injected with B16/F10-BrM cells. **B**. Flow cytometry analysis of CD63 expression
1771 gated on CD8+T cells from brains without tumor and brains intracranially injected
1772 with B16/F10-BrM cells. Error bars, s.e.m. Every dot is a different animal (n= 3
1773 metastasis free brains and n= 6 B16/F10-BrM brain metastases). The P value was
1774 calculated using the two-tailed t-test. **C.** Immunofluorescence of established
1775 B16/F10-BrM metastasis. CD63 is expressed on CD8+ T cells surrounding the
1776 lesion. Red arrow indicates a CD63+CD8+ T cell. Scale bar, 10 µm. **D.**
1777 Representative image showing colocalization of metastasis-associated CD8 and
1778 CD63 staining in a lung cancer brain metastasis patient. White arrow indicates a
1779 CD8+ T cell and red arrow indicates a double CD63+CD8+ T cell. Scale bar, 10 µm.
1780 **E.** Immunoblotting using Anti-TIMP1, Anti-CD63 and Vinculin antibodies showing
1781 secreted TIMP1 and CD63 binding on CD8+ T cells when co-cultured with pSTAT3+
1782 astrospheres. Cell lysates (first line) were immunoprecipitated with IgG isotype as
1783 control (second line) and Anti-CD63 (third line). **F.** Proximity ligation assay performed
1784 on a melanoma brain metastasis sample showing TIMP1 and CD63 in close
1785 molecular proximity on CD8+ T cells. Magnification showing red dots of TIMP1-CD63
1786 interaction (white arrows) on a CD8+ T cell highlighted with a red arrow in the main
1787 picture. Scale bar, 10 µm. **G**. Schema of the experimental design. *Wt* or CD63-null
1788 CD8+ T cells were used in *ex vivo* organotypic cultures with established B16/F10-
1789 BrM metastasis. **H.** Quantification of the BLI signal emitted by B16/F10-BrM cells in
1790 each brain slice normalized by the initial value obtained at time 0, before the addition
1791 of *wt* or CD63-null CD8+ T cells. Values are shown in box-and-whisker plots where
1792 every dot represents a different organotypic culture and the line in the box
1793 corresponds to the median. Whiskers go from the minimum to the maximum value
1794 (n = 8 no CD8+ T cells, 7 *wt* CD8+ T cells and 10 CD63-null CD8+ T cells
1795 independent organotypic cultures). Quantification is accompanied by representative
1796 images of wells containing brain organotypic cultures with established B16/F10-BrM
1797 metastases grown *ex vivo* for 24 hours. The image shows the BLI intensity in each
1798 condition for each brain slice. P values were calculated using the two-tailed t-test. **I**.
1799 Heatmap generated with the qRT-PCR analysis performed on CD63^{high}CD8+ T cells
1800 sorted from *wt* and cKO^{GFAP}-*Timp1* mice ten days after intracranial injection of
1801 B16/F10-BrM cells. n= 12 brains per condition and 6 brains for control condition (not
1802 injected with BrM cells). **J.** Schema of the experimental design. CD8+ lymphocytes
1803 were cultured with STAT3- astrospheres CM and *wt* or cKO^{GFAP}-*Timp1* STAT3+
1804 astrospheres CM and processed for phosphoproteomic analysis. **K.** Heatmap
1805 showing the top 10 enriched sequence motifs found in CD8+ T cells in the absence
1806 of TIMP1 from the CM of STAT3+ astrospheres. Clustering enrichment using Fisher
1807 Exact Test was performed. P val < 0.01 FDR < 2%. **L.** Quantification of the number
1808 of pERK+CD8+ T cells in control and cKO^{GFAP}-*Timp1* mice intracardially injected with
1809 E0771-BrM at endpoint. Error bars, s.e.m. Every dot is a different animal (n= 3 brains
1810 per condition). **M.** Quantification of the number of pERK+CD8+ T cells in human
1811 brain metastases samples scored with multiplex. Violin plots show the median of %
1812 pERK+CD8+ T cells among the total CD8+ T cells per field of view (n=5-10/patient)
1813 from 3 patients analyzed in each condition. The P value was calculated using the
1814 two-tailed t-test**. N.** Model summarizing main findings regarding the
1815 immunomodulatory role of TIMP1 derived from STAT3+ reactive astrocytes in brain
1816 metastasis. Secreted TIMP1 acts on its receptor CD63 receptor on the surface of

1817 CD8+ lymphocytes, modulating ERK mediated-signaling and downregulating
1818 activation of T cell markers and cytolytic enzymes and upregulating exhaustion
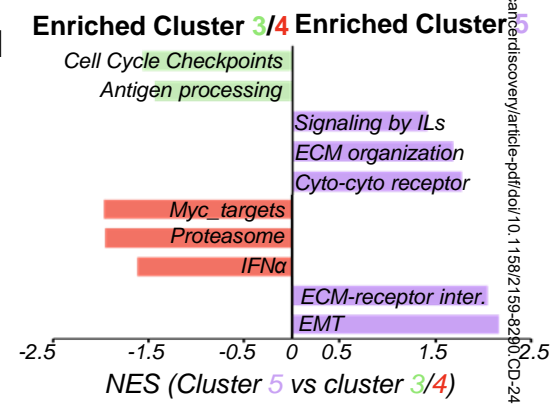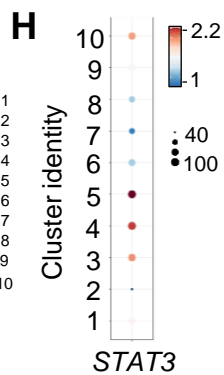1819 markers, thus affecting effective T cell-mediated killing of brain metastatic cells.
1820
1821 **Figure 7. A combined immunotherapy targeting local immunosuppression**
1822 **provides superior control of brain metastasis.**
1823 **A.** Schema of the experimental design. C57BL/6J mice were intracardially injected
1824 with B16/F10-BrM cells, after three days the following treatments were
1825 administrated: IgG2 (10 mg/kg), silibinin daily (200 mg/kg) or immune checkpoint
1826 blockade (ICB) every two days (Anti-PD1,10 mg/kg, plus Anti-CTLA4, 10 mg/kg)
1827 alone or in combination with silibinin. After two weeks, *ex vivo* analysis and
1828 histological analysis of different organs were performed. **B.** Representative images of
1829 control, ICB, silibinin and ICB plus silibinin treated mice two weeks (endpoint) after
1830 intracardiac inoculation of B16/F10-BrM cells. In *in vivo* images, dotted lines
1831 surround brain and lungs, showed in the *ex vivo* representative images below.
1832 Images show the bioluminescence (BLI) intensity. **C.** Distribution of lesions according
1833 to size (small: <5e4 μm^2, medium: 2.5e4 μm^2-2e5 μm^2, big: >2e5 μm^2). Values are
1834 represented as percentage respect to total number of lesions per each experimental
1835 condition. n= 4-6 brains per condition. P values of the different comparison
1836 calculated using the two-tailed t-test are shown in SuppTable16. **D.** Representative
1837 images of Perforin and Granzyme b staining in endpoint brains from mice treated
1838 with ICB and ICB plus silibinin. Arrows indicate positive staining. Scale bar, 50 μm. **E.**
1839 Quantification showing the number of cells expressing cytotoxic markers in D. Values
1840 are shown in box-and-whisker plots where every dot is a different lesion (n= 6
1841 lesions in 3 brains are quantified in ICB and n=4 lesions in 3 brains are quantified in
1842 ICB plus silibinin). The P value was calculated using the two-tailed t-test. **F.** Schema
1843 of the experimental design. Three days after intracranial inoculation of B16/F10-BrM
1844 cells, 5 doses of 3Gy WBRT and IgG2 (10 mg/kg), silibinin daily (200 mg/kg) or
1845 immune checkpoint blockade (ICB) every two days (Anti-PD1,10 mg/kg, plus Anti-
1846 CTLA4, 10 mg/kg) alone or in combination with silibinin were administrated. **G.**
1847 Kaplan-Meier curve showing survival proportions of mice without radiotherapy
1848 (dotted gray line, n= 12) and with radiotherapy (Rx) (IgG2 red line, n= 8; ICB blue
1849 line, n=8, silibinin gray line, n= 8, ICB+silibinin green line, n= 8). P value was
1850 calculated using log-rank (Mantel-Cox) test between Rx and Rx+ICB+silibinin
1851 groups. **H.** Representative images of cleaved-caspase 3 staining of intracranially
1852 inoculated brains with B16/F10-BrM cells at endpoint from irradiated mice treated
1853 with ICB and ICB plus silibinin. Scale bar, 75 μm, magnification 25 μm. **I.**
1854 Quantification of experiment in H. Percentage of cleaved-caspase 3 is normalized
1855 with tumor area. Values are shown in box-and-whisker plots where every dot is a
1856 different field of view. Four brains per condition are quantified. The P value was
1857 calculated using the two-tailed t-test. **J.** Representative images of Ki67- (white
1858 arrows) and Ki67+ (red arrows) CD8+ T cells infiltrating brain metastases from mice
1859 intracranially inoculated with B16/F10-BrM cells and treated with radiotherapy and
1860 either ICB or ICB plus silibinin. Scale bar, 25 μm. **K.** Quantification of experiment in
1861 J. Values are shown in box-and-whisker plots where every dot is a different field of
1862 view. Three brains per condition are quantified. The P value was calculated using the
1863 two-tailed t-test. **L.** Quantification of TIMP1 levels measured in patients´
1864 cerebrospinal fluid (CSF). Non-cancer control condition: n= 6 and brain metastasis
1865 condition: n= 12 (matched CSF samples from the same patients in FigS9A) plus n=2
1866 unmatched CSF values. Each dot is a different patient. Patients shown in N are

1867   colored in green. The P value was calculated using the two-tailed t-test. **M-N.**
1868   Schema of the strategy to perform an *ex vivo* proof of concept validation of TIMP1 as
1869   a biomarker of response to blockade of CD8+ T cell local immunosuppression.
1870   Heatmap showing immune cluster category (according to total percentage of
1871   immune cells, mean percentage of immune cells present in low immune cluster
1872   samples in Fig3G is used as reference), TIMP1 levels in the CSF (mean of TIMP1
1873   levels in the CSF of non-cancer patients is used as reference) and response to Anti-
1874   TIMP1 and Anti-TIMP1+Anti-CD8 (viability of cancer cells in percentage of Ki67^{+}
1875   cancer cells, IgG2 condition is used as reference) in PDOCs of patients in Fig7L
1876   (green dots). Results from the PDOCs are in Fig4F-G and SuppTable15.
1877   Represented values are shown in FigS9C.
1878
1879
1880

A

B16/F10-BrM

ACSA2+

scRNAseq
(7762 astrocytes)

B BrM astrocytes

UMAP_2

Stat3⁺

UMAP_1

- 0
- 1
- 2
- 3
- 4
- 5
- 6
- 7
- 8

C

Cluster identity

8 7 6 5 4 3 2 1 0

Stat3

1.5
-1

10
30

D Cluster 3

*Cell cycle-Replication-
Checkpoints*
Interferon-Antigen presentation
Cilium-Flagellum-Hedgehog
Immune response to disease
Cell-cell contact pathways
Ribosome-Translation

E Cluster 7

ECM
Cytokine signaling
Integrin signaling
Ribosome-Translation

F

Lung/breast
cancer BrM

Fixation

scRNAseq
(2612+1338
astrocytes)

G Human BrM astrocytes

UMAP_2

STAT3⁺

UMAP_1

- 1
- 2
- 3
- 4
- 5
- 6
- 7
- 8
- 9
- 10

H

Cluster identity

10 9 8 7 6 5 4 3 2 1

STAT3

2.2
1

40
100

I Enriched Cluster 3/4 Enriched Cluster 5

Cell Cycle Checkpoints
Antigen processing
Signaling by ILs
ECM organization
Cyto-cyto receptor
Myc_targets
Proteasome
IFNα
ECM-receptor inter.
EMT

-2.5   -1.5   -0.5   0   0.5   1.5   2.5

NES (Cluster 5 vs cluster 3/4)

A Astrospheres

pSTAT3- vs pSTAT3+

CD8+ T cells

B *T cell activation*

NES=-3.79 FDR=10⁻⁴

C B16/F10-BrM

Control   Silibinin

CX3CR1-
CD45+
scRNAseq
(3055 immune cells)

D

P=0.0447

% cells

- Control
- Silibinin

Cytotoxic-like T cells

E B16/F10-BrM

cKO^GFAP-*Stat3*
CD3+
CD8+
Flow
cytometry
qRT-PCR

F *Control*

CD3-APC-Cy7 / CD8-PE

SCC-A / Gzmb-PE-Cy7   8.25 %

Tmx

CD3-APC-Cy7 / CD8-PE

SCC-A / Gzmb-PE-Cy7   44.5 %

G

P=0.0127

% Gzmb+ CD8+ T cells

- Control
- Tmx

H B16/F10-BrM

cKO^GFAP-*Stat3*

αCD8

I

Control   Tmx

5x10⁴ 1x10⁶

αCD8

J

P=0.7622
P=0.0263
P=0.0344

Ex vivo brain BLI
(fold increase)

Tmx   -   +   +
αCD8   -   -   +

Figure 2

A

pSTAT3 *TIMP1*

Astrosphere

CC

Mouse brain metastasis

CC

Human brain metastasis

B

Transcriptomic data

Immune cluster

Low/ Medium/ High

n=108

García-Mulero et al.

Sensitivity

Specificity

AUC: 1.000

CD8a
CD68
ITGAX

C

STAT3 expression

P=0.045
P=0.023
P=2E-04

Immune cluster
- Low
- Medium
- High

D

TIMP1 expression

P=2E-04
P=0.004
P<1E-04

Immune cluster
- Low
- Medium
- High

E

microenv.

met

n=12

CD8/ CD68/ CD11c

pSTAT3/ *TIMP1*

?

GFAP
pSTAT3

RA

cc

F

BB CD8 CD68 CD11c

Patient #1   Patient #2   Patient #3

pSTAT3 *TIMP1*

G

TIMP1 score

% immune cells

P=0.0097

Immune cluster
- Low
- Medium
- High

H

Extracranial response   Intracranial relapse

n=8

ICB

CC

pSTAT3 *TIMP1*

CD8 GFAP pSTAT3

I

BB CC CD8 GFAP pSTAT3 GZMB

J

GZMB-CD8
GZMB+CD8
pSTAT3+ GFAP+

CD8+:pSTAT3+GFAP+

P=0.0363

GZMB-
GZMB+

1:5
1:4
1:3
1:2
1:1
1:0

Figure 3

Figure 4

A

Astrospheres

vs   *wt*
cKO^GFAP-*Timp1*

pSTAT3-   pSTAT3+

CD8+
T cells

Flow
cytometry

B

Count

CD25-PE

○ CM pSTAT3+ *wt*
● CM pSTAT3-
● CM pSTAT3+
cKO^GFAP-*Timp1*

C   Effector CD8+ T cells

CD25 gMFI
CD44+CD62L- (x10³)

P=0.0002
P=0.0002

- + - -   CM pSTAT3-
- - + -   CM pSTAT3+ wt
- - - +   CM pSTAT3+
cKO^GFAP-*Timp1*

D

%IFN-γ+TNFα+
CD8+ T cells

P=0.0432
P=0.0017

- + - -   CM pSTAT3-
- - + -   CM pSTAT3+ wt
- - - +   CM pSTAT3+
cKO^GFAP-*Timp1*

E

%PD1+LAG3+TIM3+
CD39+CD8+ T cells

P=0.0188 *P*=0.0425

- + - -   CM pSTAT3-
- - + -   CM pSTAT3+ wt
- - - +   CM pSTAT3+
cKO^GFAP-*Timp1*

F

Wild type vs
cKO^GFAP-*Timp1*

B16/F10-BrM

CD8+
T cells

G

SCC-A

wild type

22.3 %

cKO-Timp1

37.3 %

CD44-PE

H   CD8+ (*in vivo*)

% CD44^high/ CD8+

P=0.0267

wt   cKO

I

SCC-A

wild type

7.6%

cKO-Timp1

30.9%

TNFα-BV421

J   CD8+ (*in vivo*)

% TNFα+/ CD8+

P=0.0429

wt   cKO

K

PD1-VB785

wild type

cKO-Timp1

CD39 PE/Dazzle 594

L   CD8+ (*in vivo*)

% PD1+CD39+/ CD8+

P=0.0131

wt   cKO

Figure 5

A Wild type

CD63

CD8+ T cells

B16/F10-BrM

B

P=0.0404

% CD63^high/ CD8+

- + BrM

C B16/F10-BrM

CD63 CD8 BB LUC

cc

D Human brain metastasis

CD8 CD63

E pSTAT3+ astrospheres + CD8+ T cells

Input IgG IP

CD63

TIMP1

Vinculin

F Human brain metastasis

BB GFAP

CD8 TIMP1-CD63

G

CD63 TIMP1

CD8+ T cell

metastasis

CD8+ T cell

TIMP1

?

metastasis

H

Normalized BLI 24h/ 0h

P=0.0410

P=0.0457

-	+	-	*wt* CD8+ T cells
-	-	+	KO CD8+ T cells

1x10^7

1x10^6

Organotypic cultures with B16/F10-BrM mets

I CD63^high CD8+

Gzmb

Gzmk

Raw Max Min

Tumor-free wild type cKO

J

pSTAT3- pSTAT3+ wt cKO

CM

T cell

Phospho proteome

K

Kinase substrate motif enrichment factor

ERK1/2, SAPK, CDK5, GSK3

GSK3, ERK1/2,

CDK5

AMPK2

Pim1

CDK5

CDK4

RAF1

Plk1

PKG

PKA, PKG

0   1   2

L

% pERK+CD8+/ CD8+

P=0.0121

wt cKO^GFAP -*Timp1*

M

% pERK+CD8+/ CD8+

P=0.0075

Immune cluster

Low

High

Human brain metastases

N

metastasis

pSTAT3+ astrocyte

Gzm^low CD44^low Pd-1^high

CD8+ T cell

TIMP1

CD63 activation

pERK1/2

Figure 6

A

B16/F10-BrM

ICB* | Silibinin

(*) αPD-1+αCTLA-4

B

IgG | ICB | Silibinin | ICB + silibinin

in vivo

brain
lungs

10^7
10^6

ex vivo

brain/lungs | brain/lungs | brain/lungs | brain/lungs

5×10^5 1×10^4 5×10^7 5×10^6

C

Size distribution (%)

☐ Small
☐ Medium
■ Large

+	-	+	-	IgG
-	-	+	+	Silibinin
-	+	-	+	ICB

D

Gzm | Perf.

ICB

ICB + silibinin

E

Number of cytotoxic cells

P=0.0088

| - | + | Silibinin |
| + | + | ICB |

F

B16/F10-BrM

ICB* | Silibinin

(*) αPD-1+αCTLA-4

G

OS (%)

P=0.0088

0 20 25 30 35

···· No Rx
— Rx
— Rx+ICB
— Rx+silibinin
— Rx+ICB+silibinin

H

BB CC3

Rx

ICB

ICB + sil

I

% CC3+ cancer cells

P=0.00224

-	+	Sil
+	+	ICB
+	+	Rx

J

BB Ki67 CD8

Rx

ICB

ICB + sil

K

% CD8+ Ki67+ cells

P=0.00219

-	+	Sil
+	+	ICB
+	+	Rx

L

CSF TIMP1 levels (ng/ml)

P=0.0002

| + | - | Control |
| - | + | Brain mets. |

M

immune
cluster

met

microenv.

n=4

PDOC ← αTIMP1

↓ metastasis viability
CD8+ T cell-dependent

CSF → TIMP1 ELISA → ↑ TIMP1 levels

N

| | | + | + | IgG |
Reference

| | | + | + | αTIMP1 |
| | | - | + | αCD8 |

Patient#1 | | | | *na* |
Patient#2
Patient#3
Patient#4

Immune cluster (% infiltration)
6 15

CSF TIMP1 (ng/ml)
25 150

Cancer cells viability (PDOC)
0 100

Figure 7